Geochimica et Cosmochimica Acta 338 (2022) 347–364

Contents lists available at ScienceDirect

Geochimica et Cosmochimica Acta

journal homepage: www.elsevier.com/locate/gca

Limited nitrogen isotopic fractionation during core-mantle differentiation in rocky protoplanets and planets

Damanveer S. Grewal [a,b,*], Tao Sun [a], Sanath Aithala [a,c], Taylor Hough [a], Rajdeep Dasgupta [a], Laurence Y. Yeung [a,d], Edwin A. Schauble [e]

[a] Department of Earth, Environmental and Planetary Sciences, Rice University, 6100 Main Street, MS 126, Houston, TX 77005, USA
[b] Division of Geological and Planetary Sciences, California Institute of Technology, 1200 E California Blvd, Pasadena, CA 91125, USA
[c] Department of Earth and Environmental Sciences, University of Minnesota, Minneapolis, MN 55455, USA
[d] Department of Chemistry, Rice University, 6100 Main Street, MS 126, Houston, TX 77005, USA
[e] Department of Earth, Planetary, and Space Sciences, University of California, Los Angeles, CA 90095, USA

ARTICLE INFO

Article history:
Received 14 July 2022
Accepted 13 October 2022
Available online 19 October 2022
Associate editor: Mathieu Roskosz

Keywords:
Nitrogen
Core formation
Core-mantle differentiation
Isotope fractionation
Iron meteorites
Chondrites

ABSTRACT

$^{15}N/^{14}N$ ratios of meteorites are a powerful tool for tracing the journey of life-essential volatiles like nitrogen (N), carbon and water from nebular solids to the present-day rocky planets, including Earth. The utility of $^{15}N/^{14}N$ ratios of samples originating from differentiated protoplanets (e.g., iron meteorites) and planets (e.g., Earth's mantle) for tracing this journey could be affected by the fractionation of N isotopes during core-mantle differentiation, which would overprint their primitive compositions. The extent of N isotopic fractionation during core-mantle differentiation and its effect on the $^{15}N/^{14}N$ ratios of resulting metallic and silicate reservoirs is, however, poorly understood. Using high pressure–temperature experiments, here we show that equilibrium N isotopic fractionation between metallic and silicate melts ($\Delta^{15}N^{alloy-silicate} = \delta^{15}N^{alloy} - \delta^{15}N^{silicate} = -3.3$ ‰ to -1.0 ‰) is limited across a wide range of oxygen fugacity and is much smaller than previous estimates. Also, we present *ab initio* calculations based on the relevant N speciation in metallic and silicate melts confirming both the magnitude and direction of equilibrium N isotopic fractionation predicted by our experimental results. Limited N isotopic fractionation during core-mantle differentiation suggests that the core and mantle relicts largely preserve the N isotopic compositions of their bulk bodies. Based on the $\delta^{15}N$ values of non-carbonaceous iron meteorites (as low as –95 ‰), we predict that the extent of variations in the N isotopic compositions of inner solar system protoplanets was larger than that recorded by enstatite chondrites ($\delta^{15}N$ = –29 ‰ to –6‰). As most of the Earth grew primarily via the accretion of similar inner solar system protoplanets, a relatively high $\delta^{15}N$ value of present-day Earth's primitive mantle (–5‰) cannot be explained by the accretion of enstatite chondrite-like materials alone and necessitates a significant contribution of ^{15}N-rich materials to the Earth's interior.

1. Introduction

The chemical compositions of the cores and mantles of all rocky protoplanets and planets were set by core-mantle differentiation. Heat released by the decay of ^{26}Al caused large-scale melting in the earliest formed protoplanets, leading to the separation of metallic melts from partially to fully molten silicates (Hevey and Sanders, 2006; Neumann et al., 2012). Growth of large rocky planets took place via episodic collisions of differentiated protoplanets, resulting in additional core-mantle differentiation events (Rubie et al., 2011). The metallic melts equilibrated with silicate melts during their differentiation, shaping the final elemental and isotopic compositions of the cores and mantles of differentiated rocky bodies (e.g., Rubie et al., 2011; Labidi et al., 2013; Shahar et al., 2017; Bourdon et al., 2018; Dasgupta and Grewal, 2019). Comparisons of elemental and isotopic compositions amongst meteoritic and terrestrial samples have been crucial for understanding the role of core-mantle differentiation during the growth of differentiated rocky bodies in the solar system, including Earth.

As the presence of nitrogen (N), carbon (C), and water (H_2O) in the Earth's atmosphere and biosphere is critical in defining its habitability, the fate of these life-essential volatiles during the growth and differentiation of rocky bodies is of particular interest. Several lines

* Corresponding author.
E-mail address: dgrewal@caltech.edu (D.S. Grewal).

https://doi.org/10.1016/j.gca.2022.10.025
0016-7037/

of evidence suggest that these volatiles were accreted by the earliest formed rocky bodies in the inner solar system, and hence were available during the entire growth history of rocky planets. For instance, the parent bodies of non-carbonaceous (NC) iron meteorites – remnants of the cores of the earliest formed protoplanets in the inner solar system (Kruijer et al., 2014) – had N and C bearing cores (Hirschmann et al., 2021; Grewal et al., 2021c, 2022). Moreover, enstatite chondrites (ECs) – primitive meteorites from the NC reservoir that are isotopically similar to inner solar system planets in multi-isotope space – also contain hundreds of ppm of N, C, and H (Grady et al., 1986; Piani et al., 2020). Importantly, the N, C, and H isotopic compositions of these NC reservoir-derived meteorites are similar to those of Earth's primitive mantle (Javoy, 1997; Piani et al., 2020; Grewal et al., 2021c; Grewal, 2022). Therefore, N, C, and H were not only present in the seeds of the present-day rocky planets, but they also survived the planetary growth processes to contribute to the volatile budgets of these planets. As all protoplanets and planets likely underwent at least one core-mantle differentiation event during their growth, the elemental and isotopic compositions of these volatiles in their bulk silicate and core reservoirs could be overprinted by the effects of alloy melt-silicate melt equilibration. Correspondingly, determining the elemental and isotope fractionation factors of volatiles between alloy and silicate melts can yield important constraints in deciphering their origins in rocky protoplanets and planets.

The large isotopic variations amongst meteorite and terrestrial reservoirs as well as redox sensitive fractionation between alloy and silicate melts makes N a widely used proxy to probe the fate of life-essential volatiles during protoplanetary and planetary differentiation. Equilibrium elemental partitioning of N between alloy and silicate melts has been investigated extensively by several high *P-T* experimental studies over the last decade (Roskosz et al., 2013; Dalou et al., 2017; Grewal et al., 2019b, 2019a, 2021b; Speelmanns et al., 2019; Jackson et al., 2021). Although these studies have been useful in evaluating the possible causes behind the widespread depletion of N in the bulk silicate reservoirs of differentiated rocky bodies, i.e., segregation into the cores and/or atmospheric loss, they do not track the other critical constraint on the provenance of N in the rocky bodies – $^{15}N/^{14}N$ ratios.

$^{15}N/^{14}N$ ratios of primitive chondrites, differentiated meteorites, and terrestrial samples are distinct relative to the nebular gas and comets (Füri and Marty, 2015; Grewal, 2022) (Fig. 1). Combined evidence based on $^{15}N/^{14}N$, D/H, and $^{13}C/^{12}C$ isotopic ratios suggest that the parent bodies of undifferentiated and differentiated meteorites as well as rocky planets, including Earth, acquired their inventories of life-essential volatiles from a common ancestral reservoir (Marty, 2012; Alexander et al., 2017). Fingerprinting the provenance of $^{15}N/^{14}N$ ratios in differentiated rocky bodies requires ascertaining the N isotopic compositions of the bulk bodies from the $^{15}N/^{14}N$ ratios of either silicate or metallic reservoirs. For instance, the $^{15}N/^{14}N$ ratios of the primitive materials accreted by the earliest formed protoplanets in both NC and CC reservoirs have been directly inferred from the $^{15}N/^{14}N$ ratios of iron meteorites (Grewal et al., 2021c). Likewise, a resemblance of $^{15}N/^{14}N$ ratios of Earth's mantle with ECs and NC iron meteorites, and Earth's atmosphere with CC chondrites and iron meteorites, has been used as evidence for a bimodal source of N in the Earth (Javoy, 1997; Piani et al., 2020; Grewal et al., 2021c). All these conclusions rest on the assumption that the mean $^{15}N/^{14}N$ ratio of the entire differentiated body can be directly inferred from the $^{15}N/^{14}N$ ratios of a single reservoir (bulk silicate Earth (BSE) in the case of Earth, and cores in the case of iron meteorite parent bodies). For this assumption to hold, there must be insignificant differences between the $^{15}N/^{14}N$ ratios of the mantles and cores of differentiated bodies, which would only be valid if there was limited N isotope fractionation during core-mantle differentiation.

Compared to elemental partitioning, experimental data on equilibrium fractionation of N isotopes between alloy and silicate melts is limited. In a high *P-T* experimental study conducted at 1.5 GPa-1400 °C and log fO_2 = IW–3.25 to IW–0.57 (where IW stands for logfO_2 equivalent to iron-wüstite buffer), Dalou et al. (2019a) reported $\Delta^{15}N^{alloy-silicate}$ ($=\delta^{15}N^{alloy} - \delta^{15}N^{silicate}$) values varying between –243 ‰ and –25 ‰, which were positively correlated with logfO_2. Such large $\Delta^{15}N^{alloy-silicate}$ values would indicate substantial fractionation of N isotopes during core-mantle differentiation. Taken at a face value, these results would have far-reaching implications for the origin of N in rocky protoplanets and planets. First, the $\delta^{15}N$ value of Earth's primitive mantle (∼–5‰; Cartigny and Marty, 2013) could then be explained by the accretion and subsequent fractionation of EC-like material (–20.9 ‰ ± 6.2 ‰ (1σ); Grady et al., 1986) alone as N isotope fractionation during core-mantle differentiation could yield higher $^{15}N/^{14}N$ ratios in the BSE relative to ECs (Dalou et al., 2019a). Second, NC iron meteorites having lower $\delta^{15}N$ values (lower limit of –95 ‰) relative to ECs (lower limit of –27 ‰) might not capture the variation of N isotopic compositions of bulk rocky bodies in the inner solar system because their lower $^{15}N/^{14}N$ ratios could arise from N isotopic fractionation during core-mantle differentiation. Third, $\delta^{15}N$ values of achondrites like HEDs, angrites, and aubrites, as well as NC and CC iron meteorites, would not directly reflect the N isotopic compositions of their bulk bodies. Importantly, these results would imply that the provenance of N in bulk Earth (BSE + core) cannot be deduced by comparing the $^{15}N/^{14}N$ ratios of the BSE with primitive chondrites.

However, the experimental results of Dalou et al. (2019a) disagree with the theoretical and experimental results of all previous studies. Theoretical calculations accounting for redox and bond property differences (albeit not directly addressing questions related to core-mantle differentiation) predict equilibrium N isotope fractionation at high temperatures to be on the order of 1 ‰, not tens or hundreds of ‰ (e.g., Richet et al., 1977; Li et al., 2021a, 2021b). Using high *P-T* experiments to simulate core-mantle differentiation at 1.5–7 GPa, 1600–1800 °C, and logfO_2 range = IW–0.24 to IW–0.07, Li et al. (2016) reported $\Delta^{15}N^{alloy-silicate}$ values between –5.5 ‰ and –1.1 ‰, suggesting limited N isotopic fractionation during core-mantle differentiation. Due to the relatively oxidized conditions as well as a limited fO_2 range investigated in the experiments of Li et al. (2016), the possibility of large $\Delta^{15}N^{alloy-silicate}$ values as predicted by Dalou et al. (2019a) at more reduced conditions cannot be ruled out. In a recent high *P-T* experimental study at 1–8 GPa, 1700–2200 °C and logfO_2 between IW–4.72 and IW–0.31, Shi et al. (2022) reported $\Delta^{15}N^{alloy-silicate}$ values between –4.0 ‰ and +10.4 ‰. Although N isotopic fractionation between alloy and silicate melts was smaller than that of Dalou et al. (2019a), Shi et al. (2022) reported a negative correlation between $\Delta^{15}N^{alloy-silicate}$ and logfO_2. This observation is in complete contrast with the positive correlation between $\Delta^{15}N^{alloy-silicate}$ and logfO_2 reported by Dalou et al. (2019a). Importantly, Shi et al. (2022) reported positive $\Delta^{15}N^{alloy-silicate}$ values at logfO_2 < IW–1.2. This observation is in disagreement with the data of both Li et al. (2016) and Dalou et al. (2019a) where the alloy melts are shown to have lower $^{15}N/^{14}N$ ratios relative to the silicate melts. Taken together, the conflicting results of these studies fail to deliver any meaningful verdict on both the magnitude and direction of N isotope fractionation during core-mantle differentiation.

The experiments of Li et al. (2016) and Dalou et al. (2019a) had a few critical limitations. First, an approach to isotopic equilibrium-crucial for determining equilibrium fractionation of isotopes between alloy and silicate phases via high *P-T* experiments (Shahar et al., 2017) – was not demonstrated in these

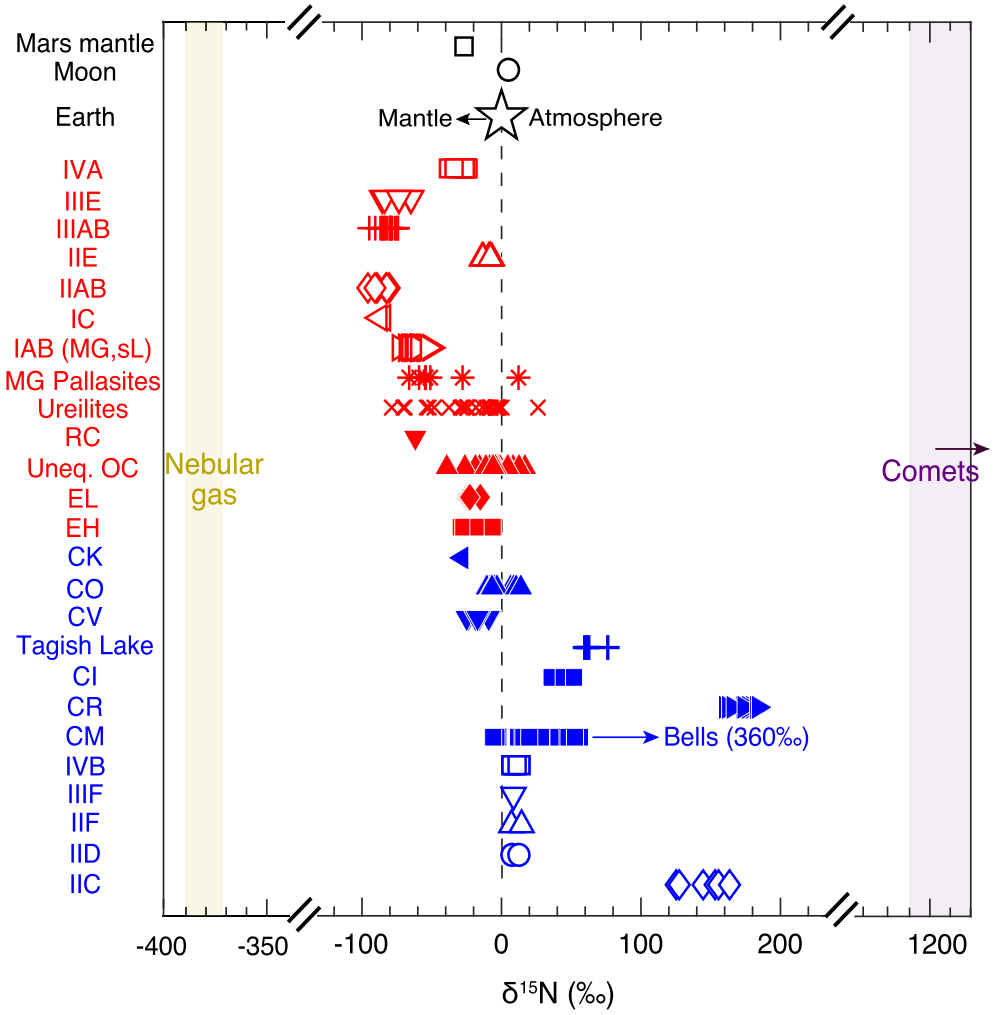

Fig. 1. Nitrogen isotopic compositions of cosmochemical reservoirs in the solar system. $\delta^{15}N$ values of bulk meteorites (chondrites, achondrites, and iron meteorites), Earth's mantle and atmosphere, Moon and Martian mantle are distinct relative to the ^{15}N-poor protosolar nebular gas and ^{15}N-rich cometary reservoirs. Meteorites are plotted in red and blue colours using the NC-CC classification based on the isotopic anomalies of Cr, Ti, and Mo (Warren, 2011; Budde et al., 2019). (For interpretation of the references to colour in this figure legend, the reader is referred to the web version of this article.)

studies. Shi et al. (2022) reported invariant $\Delta^{15}N^{alloy-silicate}$ values as a function of time, but their time-series experiments had relatively short run times (2–3 h). Second, N-bearing high *P-T* experiments simulating alloy melt-silicate melt equilibration are plagued by N loss: the quenched experimental products have significantly lower N contents relative to the starting materials (Dalou et al., 2019a; Grewal et al., 2019a, 2021b; Speelmanns et al., 2019; Jackson et al., 2021). Li et al. (2016), Dalou et al. (2019a), and Shi et al. (2022) did not evaluate the effect of N deficit in the experimental products on $\Delta^{15}N^{alloy-silicate}$. Li et al. (2016) did not report the extent of N deficit in the experimental products relative to starting materials, whereas Dalou et al. (2019a) reported significant N loss (up to ~85 %) and suggested that kinetic fractionation of N isotopes (likely via diffusion of N-vapor across the capsule walls) was a partial cause behind their large $\Delta^{15}N^{alloy-silicate}$ values. Although Shi et al. (2022) reported a lower N deficit in the experimental products relative to Dalou et al. (2019a), they did not systematically examine its effect on $\Delta^{15}N^{alloy-silicate}$. To address these experimental limitations on prior determinations of N isotope fractionation during core-mantle differentiation, a new experimental dataset is needed.

To constrain equilibrium fractionation of N isotopes between alloy and silicate melts, here we present seven sets of piston cylinder experiments (including three sets of time-series experiments, three sets of experiments with variable N in the starting mixtures, and one set of temperature-series experiments) in graphite capsules at 2–3 GPa and 1400–1800 °C. In total, 27 individual experiments were conducted. The time series experiments were used to test the approach to isotopic steady state as an indication of isotopic equilibrium. The experiments with variable amounts of N in the starting mixtures were used to constrain the effect of variable N deficit in the experimental products on $\Delta^{15}N^{alloy-silicate}$. To constrain the effect of fO_2 on $\Delta^{15}N^{alloy-silicate}$, the experiments were performed in a fO_2 range that varied over two log units (IW–3.77 to IW–1.70). This fO_2 range covers the core-mantle differentiation conditions of several rocky bodies in the solar system including iron meteorite parent bodies, Earth, Vesta, angrite parent body, and the Moon (Righter et al., 2016). To assess the quality of our experimental data, we also present the results of *ab initio* calculations based on the Density Functional Theory (DFT) to determine the magnitude and direction of equilibrium N isotopic fractionation between metallic and silicate melts at conditions relevant for core-mantle differentiation in rocky bodies.

2. Methods

2.1. Experimental details

2.1.1. Starting materials

The starting mixtures were composed of synthetic alloy mixtures containing variable amounts of Fe, Ni, N, and Si, and a mafic silicate mixture with a tholeiite basalt-like composition in 3:7 mass ratio (ThB1). To avoid the interference between fluorescence lines produced by Ti Lα and N Kα in microprobe analyses (Lengauer et al., 1992) and the formation TiN speckles (Speelmanns et al., 2019), we synthesized a TiO_2-free tholeiite basalt (ThB1) as the starting silicate mixture for our experiments (Supplementary Table 1). A similar silicate composition has been used in several alloy melt-silicate melt partitioning studies (Grewal et al., 2019a, 2019b, 2021a, 2021b). Reagent grade oxides (SiO_2, Fe_2O_3, Al_2O_3, Cr_2O_3, MnO, and MgO) and carbonates ($CaCO_3$, Na_2CO_3, and K_2CO_3) were ground and mixed under ethanol in an agate mortar for ~2–3 h. To decarbonate the carbonates, reduce Fe_2O_3 to FeO, and devolatalize the silicate mixture, it was fired in a CO-CO_2 Deltech gas mixing furnace at 1000 °C and ~ΔFMQ–2 (FMQ refers to the logfO_2 of Fayalite-Magnetite-Quartz buffer) for 24 h. For the required fO_2 conditions applicable for this study, we used Si_3N_4 as the N source in the starting materials. To test the effect of fO_2 and N loss from the capsule during the experiment, we synthesized six different alloy mixtures with varying amounts of Si and N (Supplementary Table 1). Variable amounts of reagent grade Fe, Ni, and Si metallic powders were mixed with differing amounts of Si_3N_4 under ethanol in an agate mortar for ~1 h followed by drying in dessictaor ~2–3 days to generate the alloy mixtures. Finally, the alloy and silicate mixtures were mixed in a ~3:7 ratio under ethanol in an agate mortar followed by dessicator storage for ~2–3 days.

2.1.2. Capsule material and design

Previous experimental studies that constrain partitioning of N between alloy and silicate melts have shown that all capsule designs (graphite or Pt-graphite) and materials (graphite or MgO) result in approximately similar amounts of N deficit in the experimental products relative to starting materials at identical experimental conditions (Grewal et al., 2019a, 2021b; Speelmanns et al., 2019; Jackson et al., 2021). To quench homogenous silicate glasses and maximize the amount of starting material in a given capsule (for making reliable measurements of $^{15}N/^{14}N$ ratios), the experiments were conducted in graphite capsules. Single graphite capsules have been used extensively to determine $D_N^{alloy/silicate}$ using large volume presses (Dalou et al., 2017; Grewal et al., 2019b, 2019a; Speelmanns et al., 2019; Jackson et al., 2021). It should be noted that Dalou et al. (2019a) also used single graphite capsules to determine $\Delta^{15}N^{alloy-silicate}$ values.

2.1.3. Experimental conditions

We constrained equilibrium fractionation of N isotopes between alloy and silicate melts by performing seven sets of piston cylinder experiments in graphite capsules at 2–3 GPa and 1400–1800 °C, comprising:

1) Three sets of time-series experiments demonstrating an approach to N isotopic equilibrium between alloy and silicate products. As N has only two isotopes (ruling out the utilization of the "three-isotope approach"), time-series experiments were required to demonstrate an approach to isotopic steady state, as an indication of isotopic equilibrium (Shahar et al., 2017).
2) Three sets of experiments with varying amounts of N in the starting mixtures and at two different pressures to test the effect of N loss on $\Delta^{15}N^{alloy-silicate}$. Owing to a fixed solubility of N in the alloy and silicate melts at a given *P-T-fO*$_2$, using different amounts of N in the starting materials at identical experimental conditions simulates variable N deficit in the experimental products relative to starting materials. If the missing N (i.e., N that is not present in the experimental products) was lost via diffusion across the capsule walls, its effect would be reflected in the variability on $\delta^{15}N^{alloy}$ and $\delta^{15}N^{silicate}$ values at otherwise identical conditions. However, if the $\delta^{15}N^{alloy}$ and $\delta^{15}N^{silicate}$ values were not affected by the variable N deficit in the experimental products, it would mean that the capsule acted as a closed system with efficient equilibration of N isotopes between vapor, alloy melt, and silicate melt and the missing N was finally stored in the pores of the capsule walls. Hence, these sets of experiments can be used to track the effect of N deficit in the experimental products on $\Delta^{15}N^{alloy-silicate}$ values. Out of these three sets of experiments, two were conducted at identical *P-T-fO*$_2$ to demonstrate the reproducibility of our results. It has been shown previously that there is stochasticity in the exact amount of N retained in a given set of experimental conditions (Speelmanns et al., 2019; Grewal et al., 2020, 2021b; Jackson et al., 2021). Therefore, the repeat set of experiments tests the effect of varying N deficit in the experimental products on $\Delta^{15}N^{alloy-silicate}$ values at identical *P-T-fO*$_2$ conditions.
3) One set of temperature series experiments to test the effect of *T* – known to have a strong effect on equilibrium fractionation of isotopes – on $\Delta^{15}N^{alloy-silicate}$.

In their 1.5 GPa experiments, Dalou et al. (2019a) noted a high N deficit in their experimental products (as much as 85 %), resulting in $\Delta^{15}N^{alloy-silicate}$ values that were potentially affected by kinetic isotope fractionation due to N-vapor loss across the capsule walls. Similarly high deficits of N were also observed in the relatively low *P* (0.95–1.5 GPa) experimental products of previous studies (Grewal et al., 2019a; Speelmanns et al., 2019; Jackson et al., 2021). As N deficit decreases with increasing *P* (Grewal et al., 2019a; Speelmanns et al., 2019; Jackson et al., 2021), we conducted our experiments at relatively higher pressures (2–3 GPa). For instance, Grewal et al. (2019a) showed that the percentage of N retained in the experimental products of graphite capsules increases from ~ 15 % to > 70 % with *P* increasing from 1 to 3 GPa.

As fO_2 imparts the strongest control on the variation of $D_N^{alloy/silicate}$ (Dalou et al., 2017; Grewal et al., 2019a, 2021b; Speelmanns et al., 2019; Jackson et al., 2021) and possibly on $\Delta^{15}N^{alloy-silicate}$ values (Dalou et al., 2019a; Shi et al., 2022), our experiments were performed over two log units of fO_2 range (IW–3.77 to IW–1.70). More importantly, it has been shown previously that at graphite-saturated conditions N neither exhibits strongly siderophile nor strongly lithophile behavior within the fO_2 range explored in this study [$D_N^{alloy/silicate}$ varying between ~ 0.5 to 10; (Dalou et al., 2017; Grewal et al., 2019a; Speelmanns et al., 2019; Jackson et al., 2021)]. Conducting experiments within this fO_2 range was crucial because we physically separated the quenched metallic and silicate phases for N isotopic analyses via magnetic separation after crushing. Mildly siderophile/lithophile character within the explored fO_2 range minimizes a possible contamination by micro-inclusions of alloy blebs during the silicate phase analysis, and vice-versa, to compromise our reported $\Delta^{15}N^{alloy-silicate}$ values.

2.1.4. Experimental setup

The experiments were performed using end-loaded piston cylinder (PC) devices at Rice University. A half-inch $BaCO_3$ and crushable MgO assembly with straight-walled graphite heaters following the procedural details and calibrations of Tsuno and Dasgupta (2011) was used. A Type C (W5%Re/W26%Re) thermocouple controlled and monitored the temperature. Each experiment was pressurized to the target pressure at room temperature followed by heating at a rate of 100 °C/min. Following several previous high *P-T* experimental studies of a similar type (Grewal et al., 2019b, a, 2021b, a), we sintered the experiments overnight at ~850–900 °C to reduce the porosity of the graphite capsules prior to the onset of alloy and silicate melting. The experiments were then heated to the target temperature. The experiments were quenched by cutting power to the heater thereby bringing them to the room temperature within ~10–20 s. A W-wire saw was used to cut the recovered samples longitudinally into halves. To prepare the samples for microprobe analysis, one half was mounted in Crystalbond™ followed by grinding with a 1200-grit sandpaper and polishing on a velvet cloth using a 0.3-μm alumina slurry. To remove the Crystalbond™, the polished samples were soaked overnight in acetone.

2.2. Analytical procedures

2.2.1. Electron probe micro-analysis (EPMA)

The concentrations of N along with other major and minor elements in the quenched alloy and silicate melts were measured using a JEOL JXA8530F Hyperprobe EPMA at the Department of Earth, Environmental and Planetary Sciences, Rice University. EPMA analayis has proven to be a reliable technique in measuring N in the quenched alloy and silicate melts at concentrations greater than ~70 ppm (Dalou et al., 2017; Speelmanns et al., 2019; Grewal et al., 2019b, 2019a, 2021b). Each sample was initially C-coated for silicate phase analysis. C-coated natural glasses and mineral standards (from Smithsonian Institute and SPI Supply, respectively) were used to quantify the concentrations of all elements in the silicate phase (except N). The following standards were used to measure the concentrations using the characteristic K_α X-ray lines emitted by a particular element: Si, Al, Ca, Mg, Fe, Na, K, and P - Smithsonian glasses, Cr - chromite, and Mn - rhodonite. Following several previous studies from this lab (Grewal et al., 2019b, 2019a, 2021b), BN standard was used to analyse N in the silicate glasses. A 20-μm beam at an accelerating voltage of 15 kV and a beam current of 50nA was used for silicate phase analysis with counts per second (cps) of N K_α X-rays measured using an LDE2 crystal. This analytical protocol was used for analyzing N-bearing silicate glasses in all previous studies from this lab (Grewal et al., 2019b, 2019a, 2021b). A counting time of 10 s on peak and 5 s on each background was used for all major and minor elements. Whereas, for N, the counting times on peak and each background were 80 s and 60 s, respectively, yielding a N detection limit of ~ 320 ppm in the silicate glasses.

Post-silicate phase analysis, each sample was re-polished and then Al-coated for analysis of alloy phases. Note that the alloy standard mount was also re-polished and then freshly coated with Al for each analytical session. The following standards were used for the alloy phase analysis: laboratory synthesized stoichiometric Fe_3C for C (Walker et al., 2013), natural magnetite for O, synthetic Fe, Ni and Si metals for Fe, Ni, and, Si, respectively. As reported in (Grewal et al., 2019b, 2019a, 2021b), laboratory synthesized iron nitride (Fe_3N) standard was used to obtain the concentration of N in the alloy phases. Accounting for the heterogenous texture of the quenched alloy phases, a 20-μm beam at an accelerating voltage of 12 kV and a beam current of 80 nA was used. N K_α X-rays were measured using an LDE2 crystal (following the analytical protocol of Grewal et al. (2021b, 2019a, 2019b)). Similar to the silicate glass analysis, a counting time of 10 s on peak and 5 s on each background was used for Fe, Ni, O, and Si. For N, the counting times on peak and each background were 80 s and 60 s, respectively, yielding a N detection limit of ~320 ppm in the alloy phase. Taking into consideration that C may be deposited on both standards and samples during alloy phase analysis, the standards were re-analyzed after every ~25–30 sample spot measurements on samples. An averaged value of C blank in the Fe-metal standard for a given analytical session was subtracted from the raw data to report the C concentrations in the alloy phases of samples. After the analyses of both the silicate and alloy phases, conducting coatings were removed for further N isotopic analyses.

2.2.2. Elemental Analyzer-Isotope Ratio Mass Spectrometry Analysis (EA-IRMS)

After EPMA analysis, the samples were prepared for N isotopic analyses. We avoided using secondary ion mass spectrometry (SIMS) to measure $^{15}N/^{14}N$ ratios due to the high average uncertainty (~5.5 ‰) of the *in-situ* metal analyses (Dalou et al., 2019a). Instead, we used an Elemental Analyzer-Isotope Ratio Mass Spectrometry system (EA-IRMS; ThermoScientific Flash HT Plus-Delta V Plus) to measure N isotopes in the separated phases at a higher precision. We did not perform chemical separation of the quenched alloy and silicate products to avoid potential fractionation of N isotopes during the separation process. Both halves of the uncoated samples were crushed and finely ground before the magnetic separation of alloy and silicate phases under a binocular microscope. Physical separation of the quenched alloy and silicate products has been widely used in previous studies to measure the isotopic fractionation of N (Li et al., 2016; Shi et al., 2022), S (Labidi et al., 2016), Fe (Poitrasson et al., 2009; Kubik et al., 2022), etc., in high *P-T* alloy-silicate partitioning experiments. To minimize contamination, the magnetic separation process was repeated multiple times. Each phase was analyzed for its bulk N isotope composition on an EA-IRMS at the Department of Earth, Environmental and Planetary Sciences, Rice University. 1–2 μmole of N equivalents of alloy or silicate in a given sample were weighed out and put into a tin capsule (3.5 mm × 5 mm). Subsequently the sample was analyzed in the EA-IRMS through combustion in a quartz reactor set at 1020 °C with pulse of research grade O_2 (99.999 % purity). The reactor is structured with tungstic anhydride as combustion catalyst and active copper granules as reduction reagents to achieve near 100 % conversion of target N into N_2 gas, an analyte suitable for gas-source IRMS analysis. The ammonium sulfate standards IAEA-N1 ($\delta^{15}N$ = +0.4 ‰) and IAEA-N2 ($\delta^{15}N$ = +20.3 ‰) were used for isotopic standardization. $\delta^{15}N$ values of the measurements are reported with respect to international standard air ($\delta^{15}N$ (‰) = $[(^{15}N/^{14}N)_{sample}/(^{15}N/^{14}N)_{atm} - 1] \times 1000$, where 'atm' refers to the isotopic composition of Earth's atmospheric N ($(^{15}N/^{14}N)_{atm} = 3.676 \times 10^{-3}$). Measurement precision was ±0.3 ‰ (1σ) based on multiple standard analyses spanning the analyses period (n > 20). Except for a few samples (G629, X59, G646, and X66) in which the crushed alloy or silicate phases were divided for 2–3 repeat analyses, every experiment yielded a single measurement each of the N isotopic composition of the alloy and silicate phases.

2.3. First-principles calculations

First-principles calculations based on DFT were performed to determine equilibrium mass-dependent fractionation factors of N [$1000 \bullet \ln\beta(^{15}N/^{14}N)$] for model N species in the alloy and silicate melts. $1000 \bullet \ln\beta(^{15}N/^{14}N)$ values of representative N-bearing molecules and crystals were thus used to predict the direction and magnitude of N isotopic fractionation between alloy and

silicate melts. Nitrogen is expected to be in the 0 oxidation state in metals (due to N atoms occupying interstitial voids of the metallic structure; (Goodeve and Jack, 1948)), while its oxidation state in silicates could be either 0 or −3 (Mosenfelder et al., 2019; Grewal et al., 2020). To sample the entire range of N chemistry in alloy and silicate melts as determined by previous experimental studies (Armstrong et al., 2015; Dalou et al., 2019b; Mosenfelder et al., 2019; Grewal et al., 2020), we constructed electronic structure models of several N species: Fe-rich intermetallic crystals (Fe_3N, Fe_4N, and $Fe_{16}N_2$); N_2 molecules; NH_3 molecules; molecular silicate amines with NH^{2-} ($Si_2O_6H_6NH$) and NH_2^- ($SiO_3H_3NH_2$); and anhydrous N^{3-} bearing crystals (β-Si_3N_4 and Si_2N_2O).

First-principles estimates of equilibrium mass-dependent $^{15}N/^{14}N$ fractionation factors are based on the harmonic oscillator approximation of the vibrational (or phonon) contribution to the Helmholtz free energy (Bigeleisen and Mayer, 1947); for crystals the phonon density of states is sampled on a grid of phonon wave-vectors.(e.g., Elcombe and Hulston, 1975; Méheut et al., 2007; Schauble et al., 2006). For each species, periodic DFT is used to construct model vibrational (phonon) spectra for pure ^{14}N and ^{15}N end members. All model results reported here are based on the Perdew et al. (1996) gradient corrected density functional (PBE). PBE is a widely used functional, including for previous studies of equilibrium isotope fractionation and related effects in metals, silicates, and molecules (e.g., Méheut et al., 2007; Schauble et al., 2006). Pseudopotentials and Projector Augmented Waves (PAW) are used in conjunction with plane wave basis sets. Datasets were mainly chosen from the Standard Solid State Pseudopotential collection (Prandini et al., 2021; https://www.materialscloud.org/discover/sssp/table/precision). Plane wave basis sets are cut off at a kinetic energy of 90 Ryberg (1088 eV). All DFT calculations are made using version 6.6 of the Quantum Espresso software package (Giannozzi et al., 2009; https://www.quantum-espresso.org).

Modeled species were allowed to relax to a local minimum-energy configuration, starting from previously published (measured or hypothetical) structures or structural analogues. Gas phase species were modeled as a single molecule within a cubic box of dimension 24–30 a_0 (12.7–15.9 Å), to minimize artifacts of periodic images. This treatment yields vibrational frequencies that closely match analogous *in vacuo* calculations with large atom-centred Gaussian basis sets, with RMS errors less than 1 % of the RMS vibrational frequencies for N_2, NH_3, and NH_4^+. In agreement with previous studies, frequencies for molecules and electrically insulating crystals in this study are 1–5 % lower than spectroscopic measurements (corrected for anharmonicity, in the case of N_2 and NH_3). DFT model frequencies for body-centred cubic (BCC) iron are ∼6 % higher than frequencies measured via inelastic neutron scattering (Brockhouse et al., 1967), though it is not clear whether this overestimation extends to light elements in Fe-rich alloys such as Fe_3N. Given this uncertainty, no frequency scaling has been applied. If taken at face value, the apparent systematic errors in calculated frequencies are expected to yield errors in isotopic partitioning in the direction of high $^{15}N/^{14}N$ in metallic species and low $^{15}N/^{14}N$ in other species, overestimating actual metal-silicate fractionations. For example, $1000\bullet\ln\beta(^{15}N/^{14}N)$ for N_2 is estimated to be 7.6 at 1100 °C in the present study, slightly below 7.9 as reported in Richet et al. (1977) based on anharmonically-corrected measured frequencies. A similar scaling is found for NH_3 (17.6 vs 18.7 at 500 °C) for the harmonic model by Liu and Liu (2016). Through a fortuitous cancellation of errors, a more sophisticated model from Liu and Liu (2016) that incorporates anharmonic corrections yields an estimate of 17.6, in much closer agreement with the present study; high temperature model results for NH_3 from Richet et al. (1977) seem to have artifacts that unrealistically raise estimated $1000\bullet\ln\beta$ ($^{15}N/^{14}N$) at high temperatures.

3. Results

3.1. Textures of the experimental products

The experimental products comprised metallic blobs embedded in homogenous silicate glasses (Supplementary Fig. 1A). Similar glassy textures of quenched silicate melts were also reported in both previous studies that determined isotopic fractionation of N between alloy and silicate melts (Li et al., 2016; Dalou et al., 2019a; Shi et al., 2022). The metallic alloys were composed of quenched needles of Fe,Ni-alloys, Fe,Ni-carbides, and Fe,Ni-nitrides (Dalou et al., 2017; Grewal et al., 2019b, 2019a; Speelmanns et al., 2019; Jackson et al., 2021). In agreement with previous experimental studies from the same lab containing ≤∼1.6 wt% N in the starting mixtures (Grewal et al., 2019b, 2019a, 2021b), none of the experimental products showed any signs of bubbles in the quenched alloy and silicate phases (Supplementary Fig. 1A). Rounded, homogenously distributed vesicles were, however, observed in the alloy phases of experiments with ∼2 wt% N in the starting mixtures suggesting vapor loss during quench (Supplementary Fig. 1B). Similar vesicles have also been observed in the quenched alloy phases of the experiments determining N solubility in Fe-alloy melts (Speelmanns et al., 2018).

3.2. Major and minor element compositions of alloys and silicate melts

Analogous to previous studies with similar starting mixtures (Grewal et al., 2019b, 2019a), the silicate melts had mafic compositions (NBO/T = 0.42–0.68; NBO/T is a measure of degree of silicate melt polymerization and expressed as total non-bridging oxygens per tetrahedral cations; NBO/T = (2 × Total O)/T − 4, where T = Si + Ti + Al + Cr + P). The graphite saturated alloy melts of this study were composed of Fe, Ni, C, N, and trace amounts of O and Si. The chemical compositions of the silicate and alloy melts are reported in Supplementary Tables 2 and 3, respectively.

3.3. Estimation of oxygen fugacity

Oxygen fugacity (fO_2) was determined based on the co-existence of Fe-rich alloy melt and silicate melt in the experimental products:

$$FeO^{\text{silicate melt}} = Fe^{\text{alloy melt}} + 1/2\ O_2 \quad (1)$$

where fO_2 relative to the fO_2 of iron–wüstite buffer (ΔIW), at *P-T* conditions of a given experiment, is defined as:

$$\Delta IW = 2\ \log\frac{a_{FeO}^{\text{silicate melt}}}{a_{Fe}^{\text{alloy melt}}} = 2\ \log\frac{X_{FeO}^{\text{silicate melt}}\cdot\gamma_{FeO}^{\text{silicate melt}}}{X_{Fe}^{\text{alloy melt}}\cdot\gamma_{Fe}^{\text{alloy melt}}} \quad (2)$$

where, $a_{FeO}^{\text{silicate melt}}$, $X_{FeO}^{\text{silicate melt}}$, and $\gamma_{FeO}^{\text{silicate melt}}$ are the activity, mole fraction, and activity coefficient of FeO component in the silicate phase and $a_{Fe}^{\text{alloy melt}}$, $X_{Fe}^{\text{alloy melt}}$, and $\gamma_{Fe}^{\text{alloy melt}}$ are activity, mole fraction, and activity coefficient of Fe component in the alloy phase. Non-ideal solution models ($\gamma_{FeO}^{\text{silicate melt}}$ = 1.5 (Holzheid et al., 1997) and $\gamma_{Fe}^{\text{alloy melt}}$ determined via the 'Online Metal Activity Calculator' (https://www.earth.ox.ac.uk/∼expet/metalact) were used to report fO_2 relative to the IW buffer.

3.4. Nitrogen contents in alloy and silicate melts

The three sets of time series (2 GPa/1600 °C, 3 GPa/1600 °C, and 3 GPa/1700 °C; 1–24 h duration) experiments show no correlation between experimental duration and N contents in the alloy and silicate melts, $D_N^{\text{alloy/silicate}}$, and silicate melt composition (represented

by NBO/T) (Supplementary Fig. 2). Similar obervations can be made for the set of temeparture series experiments (Supplementary Fig. 3). The three sets of experiments with variable amounts of N in the starting mixtures (two at 2 GPa/1600 °C and one at 3 GPa/1600 °C) show that at a given *P*, N contents in both alloy and silicate melts increase with increasing N content in the starting mixture (Supplementary Fig. 4A, B). For the alloy melts, this positive correlation holds for the entire range of starting N contents explored in this study, i.e., up ~2 wt% N. For the silicate melts, the positive correlation holds up to ~1.5 wt% N in the starting mixture, beyond which the N contents plateau. However, $D_N^{alloy/silicate}$ values do not show any correlation with N content of the starting mixture (Supplementary Fig. 4C).

All three sets of time series experiments show no correlation between the percentage of N retained in the quenched alloy and silicate phases and the experimental duration (p-values for 2 GPa/1600 °C, 3 GPa/1600 °C, and 3 GPa/1700 °C sets of experiments are 0.15, 0.42, and 0.67, respectively) (Fig. 2A). The percentage of N retained also does not show any correlation with the amount of N in the starting mixture (Fig. 2B). The two sets of identical experiments at 2 GPa/1600 °C have almost identical amounts of N retained in the quenched alloy and silicate phases. The temperature series experiments show that the amount of N retained does not vary significantly with *T* and time despite the longer duration of the 1400–1500 °C (72 h) experiments than those at 1800 °C (1 h) (Fig. 2C). The 3 GPa experiments generally retain higher amounts of N than those conducted at 2 GPa (Fig. 2D). Additionally, at a given *P* the amount of N retained does not show any correlation with fO_2 (p-values for 2 GPa/1600 °C, 3 GPa/1600 °C, and 3 GPa/1700 °C sets of experiments are 0.18, 0.48, and 0.19, respectively) – the parameter that primarily controls equilibrium partitioning of N between alloy and silicate melts. Overall, the $D_N^{alloy/silicate}$ values of this study vary between ~0.5 and 16. The data for equilibrium partitioning of N between alloy and silicate melts of this study follow the previously reported trend of a decrease in $D_N^{alloy/silicate}$ with decreasing fO_2 (Fig. 3) (Roskosz et al., 2013; Li et al., 2016; Dalou et al., 2017, 2019a; Grewal et al., 2019b, 2019a, ,2021b; Speelmanns et al., 2019; Jackson et al., 2021; Shi et al., 2022).

3.5. Nitrogen isotopes in alloy and silicate melts

$\delta^{15}N^{alloy}$ values of this study vary between −8.4 ‰ and −7.2 ‰ (±0.3 ‰; 1σ based on replicate standard analyses) and $\delta^{15}N^{silicate}$ values between −6.6 ‰ and −5.3 ‰ (±0.3 ‰; 1σ) (Table 1). The resulting $\Delta^{15}N^{alloy-silicate}$ values vary between −3.3 ‰ and −1.0 ‰ (±0.4 ‰; 1σ). Alloy melts had consistently lower $\delta^{15}N$ values than the equilibrating silicate melts. The replicate analyses (2–3) of the alloy and silicate phases for a few experiments yielded a pooled standard deviation of ±0.04 ‰ (1σ), which is smaller, but ultimately consistent with the observed reproducibility of the isotope standards (Supplementary Fig. 5). Measurements of N isotopic ratios in the alloy and silicate phases therefore do not show additional variability beyond that expected from analytical uncertainty. The three sets of time series experiments show that neither $\delta^{15}N^{alloy}$ nor $\delta^{15}N^{silicate}$ values correlate with experiment duration (p-values of $\delta^{15}N^{alloy}$ and $\delta^{15}N^{silicate}$ > 0.13 and 0.09, respectively, for all sets of experiments) (Fig. 4A, B, C). As a result, the $\Delta^{15}N^{alloy-silicate}$ values do not vary substantially from the shortest (1 h) to the longest experiment duration (24 h) (Fig. 5A). The $\Delta^{15}N^{alloy-silicate}$ values of the three time series experiments do not show any systematic variation with change in *P* and *T* for a given experiment duration (Fig. 5A). The three sets of experiments with varying amounts of N in the starting mixtures also have almost identical $\Delta^{15}N^{alloy-silicate}$ values (Fig. 5B). No significant

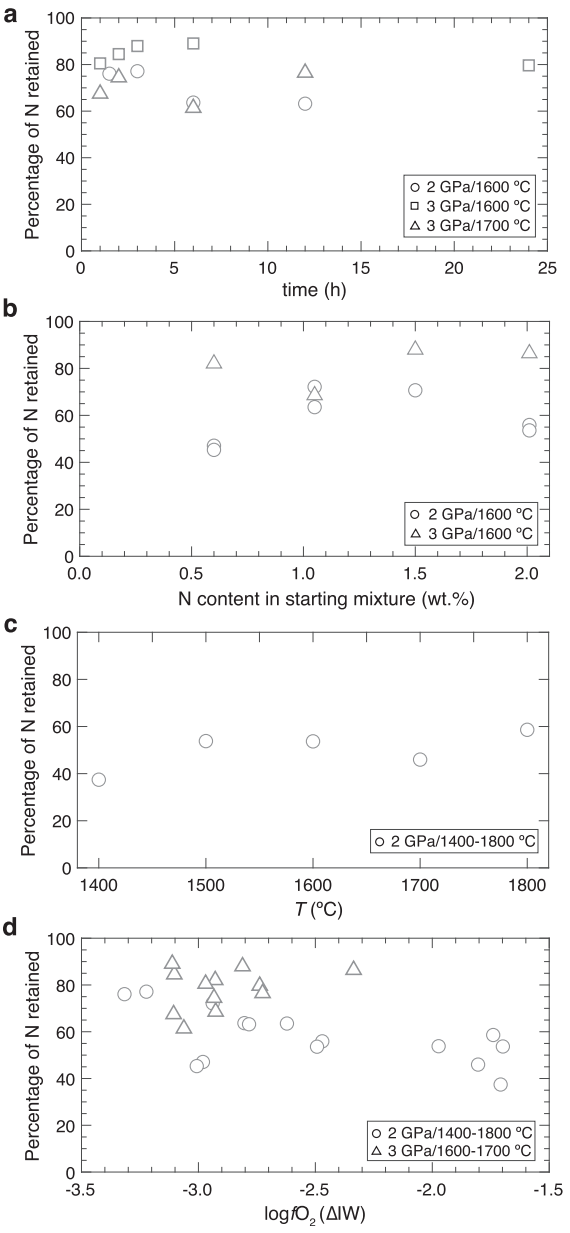

Fig. 2. Average percentage of N retained in the quenched alloy and silicate phases as a function of **A)** time, **B)** N content of the starting mixtures, **C)** temperature, and **D)** fO_2. Percentage of N retained does not show any correlation with experimental duration, *T*, and fO_2. The 3 GPa experiments generally retained a higher percentage of N relative to those conducted at 2 GPa.

difference (p-value = 0.06) was observed between the $\Delta^{15}N^{alloy-silicate}$ values at 2 and 3 GPa for a given amount of N in the starting mixture. Importantly, amongst these experiments were two sets conducted at identical *P-T* conditions; their results were indistinguishable, attesting to the reproducibility of the $\Delta^{15}N^{alloy-silicate}$ values in this study. The temperature series experiments show that there was no substantial variation (p-value = 0.21) of $\Delta^{15}N^{alloy-silicate}$ values as a function of *T* (Fig. 5C). The $\Delta^{15}N^{alloy-silicate}$ values of the temperature series experiments, which were conducted at relatively oxidized conditions ($logfO_2$ between IW–1.97 and IW–1.70), are ~1 ‰ lower than the other six sets of experiments which were more reduced ($logfO_2$ between IW–3.32 and IW–2.34). $\Delta^{15}N^{alloy-silicate}$ values do not show any correlation with the percentage of N retained in the experimental products for all seven sets of experiments (Fig. 6A, B, C). It must be noted that even

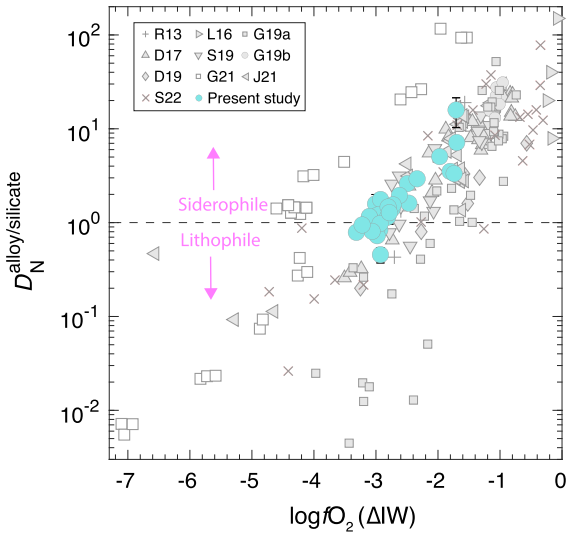

Fig. 3. $D_N^{alloy/silicate}$ as a function of fO_2. $D_N^{alloy/silicate}$ values of this study follow the well-defined correlation where the siderophile character of N decreases with decreasing fO_2. Within a similar fO_2 range, $D_N^{alloy/silicate}$ values of this study determined in graphite capsules lie within the range defined by previously determined values for graphite saturated alloys (symbols filled with grey colours) but are an order of magnitude lower than C-poor alloys (empty squares). Error bars for $D_N^{alloy/silicate}$ values of this study represent ± 1-σ deviation obtained by propagation of ± 1-σ deviation on N contents in alloy and silicate melts. Where absent, the error bars are smaller than the symbol size. Data sources: R13 - Roskosz et al. (2013); L16 - Li et al. (2016); D17 - Dalou et al. (2017); G19a - Grewal et al. (2019a); G19b - Grewal et al. (2019b); D19 – Dalou et al. (2019a); S19 - Speelmanns et al. (2019); G21- Grewal et al. (2021b); J21 - Jackson et al. (2021); S22 - Shi et al. (2022).

though a higher amount of N was retained in 3 GPa experiments relative to those at 2 GPa under otherwise identical conditions (Fig. 2B), their $\Delta^{15}N^{alloy-silicate}$ values lie in a similar range (Fig. 6B).

3.6. Density Functional Theory calculations

Temperature-dependent 1000•lnβ($^{15}N/^{14}N$) values of the modelled N species are plotted in Fig. 7. 1000•lnβ($^{15}N/^{14}N$) values increase from ~0 with decreasing temperature, with the maximum fractionation being less than 8 ‰ for N_2 at 1400 K. There are substantial differences in 1000•lnβ($^{15}N/^{14}N$) values of the modelled N species in the metal and silicates. Across the entire T range appliable for core-mantle differentiation in rocky protoplanets and planets, Fe-rich intermetallic crystals (Fe_3N, Fe_4N, and $Fe_{16}N_2$) have lower 1000•lnβ($^{15}N/^{14}N$) values than N_2 molecules, NH_3 molecules, molecular silicate amines with NH^{2-} ($Si_2O_6H_6NH$) and NH_2^- (SiO_3-H_3NH_2), and anhydrous N^{3-} bearing crystals (β-Si_3N_4 and Si_2N_2O). Also note the variability in the 1000•lnβ($^{15}N/^{14}N$) values of N-bearing silicate species.

4. Discussion

4.1. Elemental partitioning of nitrogen between alloy and silicate melts

The three sets of time series experiments demonstrate that $D_N^{alloy/silicate}$ values do not show any correlations with experimental duration (Supplementary Figs. 2, 3). Also, there was no spatial zonation of N contents in the quenched alloy and silicate phases. The combined evidence, in agreement with previous studies (Dalou et al., 2017; Grewal et al., 2019b, 2019a; Speelmanns et al., 2019; ,2021b; Jackson et al., 2021), suggests that $D_N^{alloy/silicate}$ values approached steady state within 1 h. The plateauing of N contents in alloy melts containing greater than ~1.5 wt% N in the starting mixture can be explained if the alloys were saturated in a N-rich vapor phase (Supplementary Fig. 4A). The empirical model of Speelmanns et al. (2018) predicts that N solubility in graphite-saturated alloy melts is ~1.9 wt% at 2 GPa and ~2.9 wt% at 3 GPa. N contents in the alloy melts with ~2 wt% N in the starting mixture fall within the range of the N solubility values at both 2

Table 1
Summary of the experimental conditions, quench products, oxygen fugacity, and elemental and isotopic fractionation of nitrogen (N):

Run No.	P (GPa)	T (°C)	Duration (hrs.)	Starting compositions	Capsule	Quench Products	log fO_2 (ΔIW)	$D_N^{alloy/silicate}$ Mean	$D_N^{alloy/silicate}$ 1-σ	$\delta^{15}N^{alloy}$ (‰)	$\delta^{15}N^{silicate}$ (‰)	$\Delta^{15}N^{alloy-silicate}$ (‰)
G577	2	1400	72	70 %ThB1 + 30 %Fe-5Ni-5 N-7.5Si	Graphite	Glass + Alloy	−1.71	15.8	5.6	−8.2	−5.8	−2.4
X19	2	1500	72	70 %ThB1 + 30 %Fe-5Ni-5 N-7.5Si	Graphite	Glass + Alloy	−1.97	5.1	0.4	−7.6	−5.4	−2.2
G576	2	1600	24	70 %ThB1 + 30 %Fe-5Ni-5 N-7.5Si	Graphite	Glass + Alloy	−1.70	7.1	1.1	−8.1	−5.3	−2.8
B452	2	1700	2	70 %ThB1 + 30 %Fe-5Ni-5 N-7.5Si	Graphite	Glass + Alloy	−1.80	3.5	0.3	−8.4	−5.8	−2.5
X18	2	1800	1	70 %ThB1 + 30 %Fe-5Ni-5 N-7.5Si	Graphite	Glass + Alloy	−1.74	3.3	0.5	−7.9	−5.2	−2.7
G629	2	1600	4	70 %Thb1 + 30 %Fe-5Ni-10Si-6.7 N	Graphite	Glass + Alloy	−2.47	1.6	0.1	−7.8	−6.4	−1.4
G630	2	1600	4	70 %Thb1 + 30 %Fe-5Ni-10Si-3.5 N	Graphite	Glass + Alloy	−2.94	0.8	0.1	−7.9	−6.5	−1.4
X57	2	1600	4	70 %Thb1 + 30 %Fe-5Ni-10Si-2 N	Graphite	Glass + Alloy	−2.98	0.7	0.1	−7.8	−6.6	−1.2
G653	2	1600	4	70 %Thb1 + 30 %Fe-5Ni-10Si-6.7 N	Graphite	Glass + Alloy	−2.49	2.6	0.3	−8.1	−6.2	−1.9
G655	2	1600	4	70 %Thb1 + 30 %Fe-5Ni-10Si-3.5 N	Graphite	Glass + Alloy	−2.62	1.9	0.3	−8.0	−6.4	−1.6
G654	2	1600	4	70 %Thb1 + 30 %Fe-5Ni-10Si-2 N	Graphite	Glass + Alloy	−3.01	1.6	0.4	−8.1	−6.8	−1.3
X58	3	1600	4	70 %Thb1 + 30 %Fe-5Ni-10Si-6.7 N	Graphite	Glass + Alloy	−2.34	2.9	0.3	−7.9	−6.2	−1.7
X59	3	1600	4	70 %Thb1 + 30 %Fe-5Ni-10Si-3.5 N	Graphite	Glass + Alloy	−2.93	1.8	0.1	−7.9	−6.3	−1.6
X60	3	1600	4	70 %Thb1 + 30 %Fe-5Ni-10Si-2 N	Graphite	Glass + Alloy	−2.93	0.5	0.1	−7.7	−6.3	−1.4
X61	3	1600	1	70 %Thb1 + 30 %Fe-5Ni-5 N-10Si	Graphite	Glass + Alloy	−2.97	1.2	0.1	−7.8	−6.4	−1.4
G646	3	1600	2	70 %Thb1 + 30 %Fe-5Ni-5 N-10Si	Graphite	Glass + Alloy	−3.10	1.1	0.1	−7.8	−6.4	−1.4
G592	3	1600	3	70 %Thb1 + 30 %Fe-5Ni-5 N-10Si	Graphite	Glass + Alloy	−2.81	1.1	0.1	−7.7	−6.5	−1.2
G645	3	1600	6	70 %Thb1 + 30 %Fe-5Ni-5 N-10Si	Graphite	Glass + Alloy	−3.11	0.9	0.1	−7.5	−6.5	−1.0
X66	3	1600	24	70 %Thb1 + 30 %Fe-5Ni-5 N-10Si	Graphite	Glass + Alloy	−2.74	1.4	0.1	−7.5	−6.3	−1.2
G650	3	1700	1	70 %Thb1 + 30 %Fe-5Ni-5 N-10Si	Graphite	Glass + Alloy	−3.11	1.2	0.1	−7.2	−6.0	−1.2
G647	3	1700	2	70 %Thb1 + 30 %Fe-5Ni-5 N-10Si	Graphite	Glass + Alloy	−2.93	1.0	0.1	−7.6	−6.2	−1.4
G651	3	1700	6	70 %Thb1 + 30 %Fe-5Ni-5 N-10Si	Graphite	Glass + Alloy	−3.06	0.8	0.1	−7.4	−6.0	−1.4
G652	3	1700	12	70 %Thb1 + 30 %Fe-5Ni-5 N-10Si	Graphite	Glass + Alloy	−2.73	1.5	0.1	−7.2	−5.8	−1.4
G593	2	1600	1.5	70 %Thb1 + 30 %Fe-5Ni-5 N-10Si	Graphite	Glass + Alloy	−3.32	0.8	0.1	−8.0	−6.9	−1.1
G591	2	1600	3	70 %Thb1 + 30 %Fe-5Ni-5 N-10Si	Graphite	Glass + Alloy	−3.22	0.9	0.1	−8.0	−7.0	−1.0
G656	2	1600	6	70 %Thb1 + 30 %Fe-5Ni-5 N-10Si	Graphite	Glass + Alloy	−2.80	1.5	0.2	−8.0	−6.9	−1.1
G657	2	1600	12	70 %Thb1 + 30 %Fe-5Ni-5 N-10Si	Graphite	Glass + Alloy	−2.78	1.3	0.3	−8.1	−6.6	−1.5

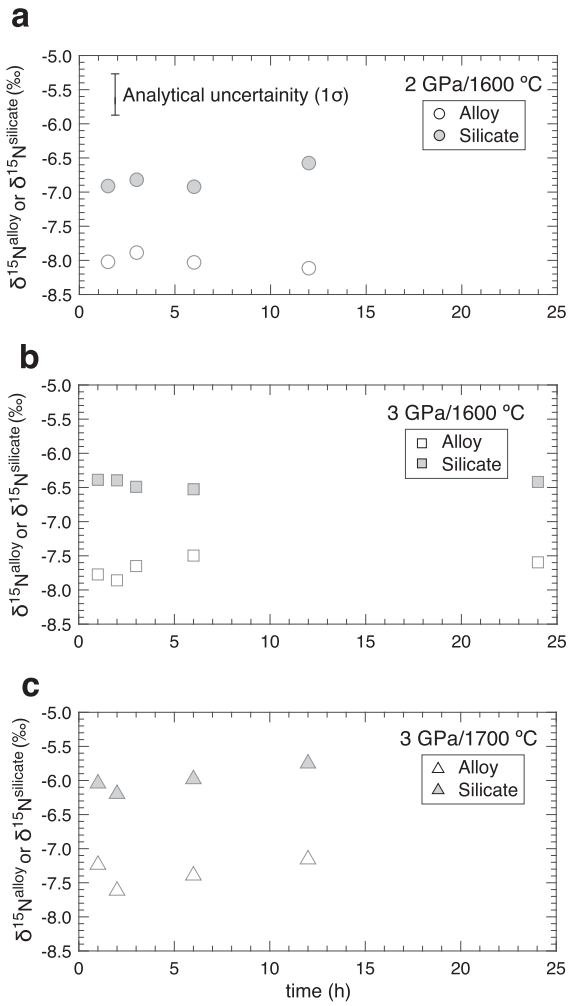

Fig. 4. $\delta^{15}N^{alloy}$ and $\delta^{15}N^{silicate}$ as a function of time for the three time-series experiments. N isotopic compositions of the alloy and silicate melts of all three time-series experiments do not vary with experimental duration. Analytical uncertainty (1σ) of the $\delta^{15}N$ values is ± 0.3 ‰.

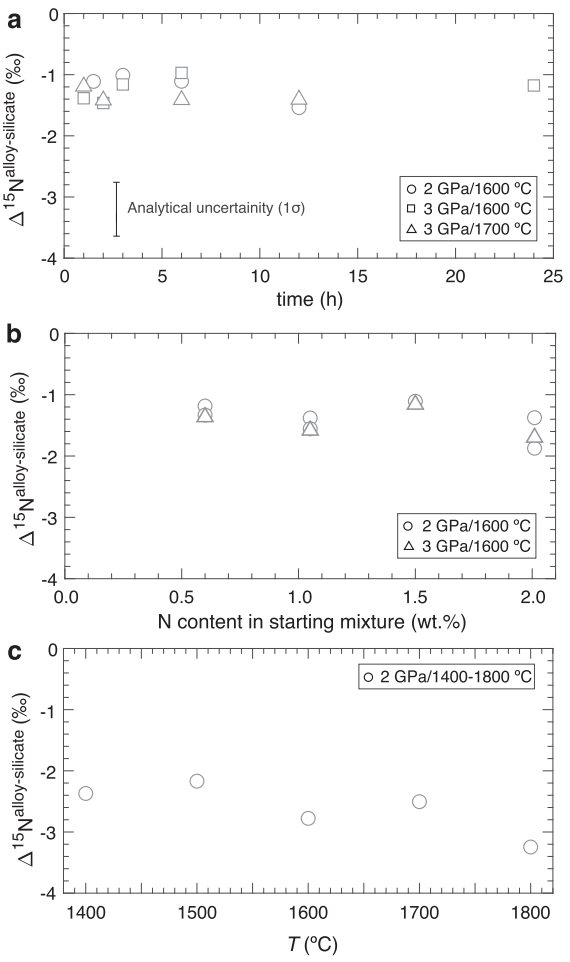

Fig. 5. $\Delta^{15}N^{alloy-silicate}$ as a function of **A)** time, **B)** N content of the starting mixtures, and **C)** temperature. For a given series of experiments, $\Delta^{15}N^{alloy-silicate}$ values of this study do not show any clear correlation with experimental duration, N content in starting mixture, *P*, and *T*. Also, panel **B)** represents the $\Delta^{15}N^{alloy-silicate}$ values of two sets of experiments which were conducted at identical conditions (represented by circles). Almost identical $\Delta^{15}N^{alloy-silicate}$ values of these two sets of experiments exhibits the reproducibility of our experimental results. Uncertainty (1σ) of ± 0.4 ‰ is obtained by propagating the uncertainty in $\delta^{15}N^{alloy}$ and $\delta^{15}N^{silicate}$ values.

and 3 GPa indicating that the N contents in alloy melts of these experiments likely reached their vapor saturation limits (Supplementary Fig. 4A). This inference is supported by the observation of homogenous, rounded vesicles in the quenched alloy melts of experiments containing ~2 wt% N in the starting mixtures (Supplementary Fig. 1B). Note that the alloy melts of this study are graphite-saturated and N solubility in graphite-saturated alloy melts is lower than that of C-poor alloy melts (Speelmanns et al., 2018). At a fixed N content in the starting mixtures, N abundances in the alloy melts, in agreement with Sievert's Law ($[N]^{alloy\ melt} \propto \sqrt{p_{N_2}}$) and previous high *P-T* experimental studies (Speelmanns et al., 2018; Dasgupta et al., 2022), increase with increasing *P* (Supplementary Fig. 4A). At a given fO_2, N abundances in the silicate melts also show a similar behavior (Supplementary Fig. 4B). An increase of N contents in both alloy and silicate melts with increasing N content in the starting mixtures and *P* results in them having no apparent correlation with $D_N^{alloy/silicate}$ values (Supplementary Fig. 4C). Importantly, a lack of variation of $D_N^{alloy/silicate}$ values with increasing N content of the starting mixtures means that $D_N^{alloy/silicate}$, unlike $D_C^{alloy/silicate}$ (Grewal et al., 2021a), does not depend on bulk N content available during core-mantle differentiation. This observation is supported by the observation that the $D_N^{alloy/silicate}$ values determined by Shi et al. (2022) for relatively N-poor systems (containing ~1000–2000 ppm N in starting materials) are approximately similar to the experimental data of previous studies containing ~1–2 wt% level N in the starting mixtures (Fig. 3). This suggests that partitioning of N between alloy and silicate melts follows Henrian behavior, i.e., activity coefficients of N in the alloy and silicate melts do not change significantly with its bulk concentration. Therefore, experimentally determined $D_N^{alloy/silicate}$ values for systems containing wt.% level N are directly applicable for core-mantle differentiation in rocky bodies containing few tens to hundreds of ppm of bulk N.

A lack of correlation between the percentage of N retained in the quenched alloy and silicate phases and the experimental duration suggests that there was no continuous loss of N-bearing vapor across the capsule walls over time (Fig. 2A). Even though there is stochasticity in the exact amount of N retained, almost identical amounts of N retained in the quenched alloy and silicate phases of the two sets of identical experiments at 2 GPa/1600 °C demonstrates the reproducibility of our experimental results (Fig. 2B). Despite the overall variability in the amounts of N retained under otherwise similar conditions at 2 and 3 GPa, a comparison of the

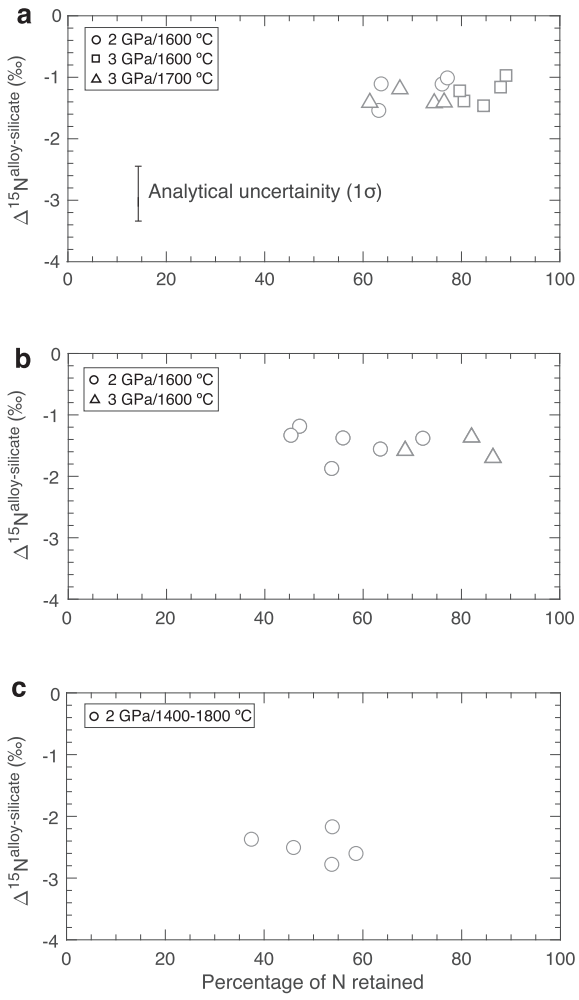

Fig. 6. $\Delta^{15}N^{alloy-silicate}$ as a function of percentage of N retained for: A) three sets of time-series experiments; B) three sets of experiments with different amounts of N in the starting mixtures, C) one set of temperature-series experiments. $\Delta^{15}N^{alloy-silicate}$ of this study do not show any correlation with the percentage of N retained despite variable amounts of N loss in all seven series of experiments. Even though the 3 GPa experiments retain higher amounts of N relative to those conducted at 2 GPa, their $\Delta^{15}N^{alloy-silicate}$ are approximately similar.

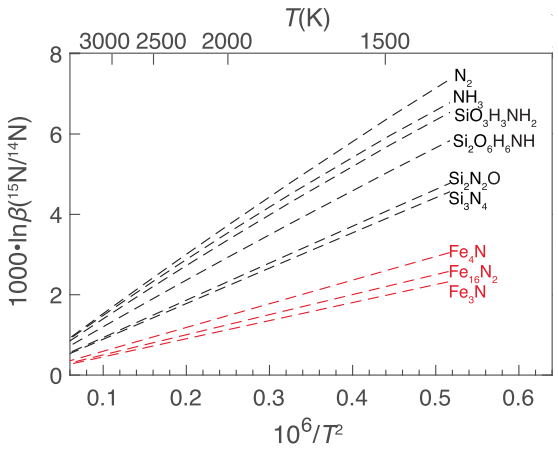

Fig. 7. Calculated $1000\bullet\ln\beta(^{15}N/^{14}N)$ values of the modelled N species in the alloys and silicates as a function of temperature. $1000\bullet\ln\beta(^{15}N/^{14}N)$ values of all N bearing metal species are isotopically lighter than the silicate species.

$\delta^{15}N^{alloy}$, $\delta^{15}N^{silicate}$, and $\Delta^{15}N^{alloy-silicate}$ values between 2 and 3 GPa experiments at otherwise identical conditions should provide a direct test of whether kinetic isotope fractionation driven by N vapor loss across the capsule walls affected the equilibrium fractionation of N isotopes between alloy and silicate melts in this study. Overall, ~38 to 89 % of N (average = ~67 %) was retained in the quenched alloy and silicate phases of this study. These fractions of N retained in single-graphite-capsule experiments at 2–3 GPa are similar to or higher than those in the experimental products of previous studies. Grewal et al. (2019a) reported 12–95 % N retention (average = ~52 %) in single-graphite and double-Pt-graphite capsule experiments at 1–7 GPa. Speelmanns et al. (2019) reported ~9 to 88 % N retention (average = ~58 %) in double Pt-graphite and Ir-graphite capsule experiments at 0.85–5.5 GPa. Jackson et al. (2021) reported 4–49 % N retention in single graphite capsule experiments at 0.95–2.38 GPa. Grewal et al. (2021b) reported 50–78 % N retention (average = ~62 %) in single MgO capsule experiments at 3 GPa. It must be noted that the percentage of N retained in the quenched alloy and silicate phases of the present study is substantially higher than the single graphite capsule experiments of Dalou et al. (2019a) at 1.5 GPa (14–42 %; average = ~25 %). In comparison to all previous studies for N-rich systems, Shi et al. (2022), using double Pt-graphite and Pt-zirconia capsules as well as single graphite capsules, reported extremely high percentage of N retained in their experimental products under N-poor conditions. Surprisingly, most of their experimental products contain more N (sometimes greater than by a factor of two) than what was added into the starting materials.

Within the fO_2 range of this study, the $D_N^{alloy/silicate}$ values are consistent with the previous data obtained from graphite capsules. The $D_N^{alloy/silicate}$ of the graphite-saturated alloys in this study are an order of magnitude lower than the C-poor alloys of Grewal et al. (2021b) due to an increase in $\gamma_N^{alloy\ melt}$ (activity coefficient of N in the alloy melt with infinitely dilute solution as the standard state) with increasing C content in the alloy melts. It can be clearly seen that despite the vast range of experimental parameters explored in this study and previous studies (P = 0.85 to 25.6 GPa, T = 1400 to 3164 °C, logfO_2 = IW–7.1 to IW–0.2, S content of alloy = 0 to 32.1 wt%, Si content of alloy = 0 to 24.6 wt%, NBO/T = 0.4 to 2.5 and C content of alloy = 0.1 wt% to graphite-saturated), $D_N^{alloy/silicate}$ is primarily controlled by fO_2.

4.2. Isotopic fractionation of nitrogen between alloy and silicate melts

Neither the $\delta^{15}N^{alloy}$ and $\delta^{15}N^{silicate}$ values nor the $\Delta^{15}N^{alloy-silicate}$ values varied substantially as a function of experimental duration in the time series experiments (Figs. 4 and 5A). This observation suggests that there was no net exchange of N isotopes between alloy and silicate melts at timescales more than 1 h at 2–3 GPa and 1600–1700 °C. As all experiments in this study had a run time greater than or equal to 1 h, $\delta^{15}N^{alloy}$, $\delta^{15}N^{silicate}$, and $\Delta^{15}N^{alloy-silicate}$ values of this study reached their steady state. A lack of correlation between $\Delta^{15}N^{alloy-silicate}$ values and percentage of N retained in the quenched alloy and silicate phases suggests that variable N deficit in the experimental products did not affect the extent and direction of N isotopic fractionation between alloy and silicate melts in the P-T-fO_2-X space explored in this study (Fig. 6). This observation is in sharp contrast to that of Dalou et al. (2019a) where they observed correlations between $\delta^{15}N^{silicate}$ (or the resulting $\Delta^{15}N^{alloy-silicate}$) values and the percentage of N retained. Also, the $\Delta^{15}N^{alloy-silicate}$ values are independent of the initial N contents of the starting mixtures (Fig. 5B). The combined evidence suggests that similar to the elemental partitioning of N, its isotopic exchange between alloy and silicate melts had likely approached its steady state for all experimental products.

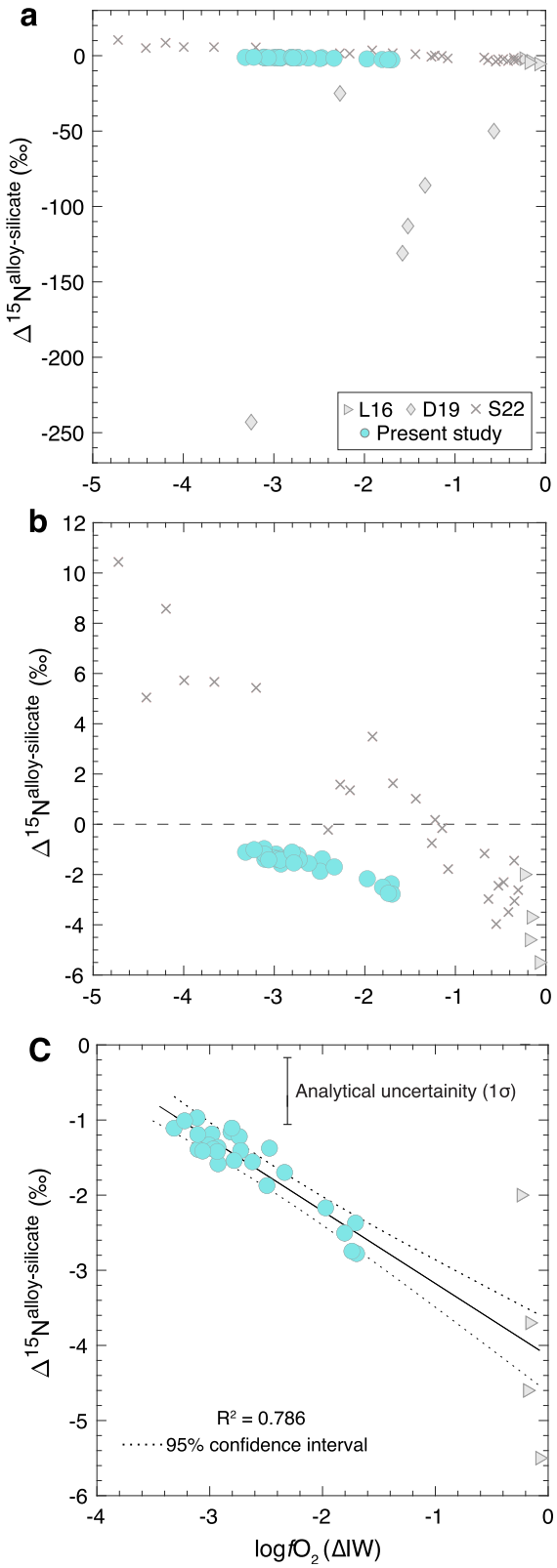

The direction of fractionation of N isotopes between alloy and silicate melts observed in this study, i.e., alloy melts having lower $\delta^{15}N$ values relative to the silicate melts, is consistent with the results of Dalou et al. (2019a) and Li et al. (2016) across the entire fO_2 space (IW–3.77 to IW–1.70) (Fig. 8A). This observation is in contrast with the data of Shi et al. (2022) at $\log fO_2$ < IW–1.2, where the alloy melts were reported to exhibit higher $\delta^{15}N$ values than the silicate melts (Fig. 8B). The $\Delta^{15}N^{alloy-silicate}$ values of this study (–3.3 ‰ to –1.0 ‰) are markedly more subdued than the data of Dalou et al. (2019a) (–243 ‰ to –25 ‰) but lie within the range of Li et al. (2016) (–5.5 ‰ to –1.1 ‰) and Shi et al. (2022) (–4.0 ‰ to +10.4 ‰). In agreement with Shi et al. (2022), the $\Delta^{15}N^{alloy-silicate}$ values of this study show a negative correlation with $\log fO_2$, albeit with a limited range (Fig. 8B,C). This negative correlation suggests that similar to elemental fractionation of N between alloy and silicate melts, N isotope fractionation between alloy and silicate melts is controlled by fO_2 within the *P-T-*fO_2*-X* space explored in this study. It is important to note that in addition to the range of variation, the negative correlation between $\Delta^{15}N^{alloy-silicate}$ and $\log fO_2$ observed in this study is in clear disagreement with the positive correlation observed by Dalou et al. (2019a).

4.3. Effect of N-vapor loss on nitrogen isotopic fractionation between alloy and silicate melts

Similar to all previous studies that constrained elemental (Roskosz et al., 2013; Dalou et al., 2017; Grewal et al., 2019b, 2019a; Speelmanns et al., 2019; ,2021b; Jackson et al., 2021) and isotopic fractionation (Li et al., 2016; Dalou et al., 2019a; Shi et al., 2022) of N, the experimental products of this study exhibited a N deficit relative to the starting materials (Fig. 2). Despite variable N deficit, $D_N^{alloy/silicate}$ values of this study and all previous studies across different labs using different capsule materials and designs follow common correlations with thermodynamic parameters like fO_2 (Fig. 3). Is the isotopic fractionation of N between alloy and silicate melts, analogous to its elemental partitioning, unaffected by variable N loss? Li et al. (2016) did not report the extent of N deficit in their experimental products; therefore, the effect of N loss on $\Delta^{15}N^{alloy-silicate}$ values cannot be ascertained from their data. Shi et al. (2022) reported limited N deficit (even a N excess in most of their experiments) in their experimental products and did not observe any effect of this parameter on their $\Delta^{15}N^{alloy-silicate}$ values. Dalou et al. (2019a) reported an anomalously high N deficit in their experimental products, and the authors reported their $\delta^{15}N^{silicate}$ values to be affected by N loss following Rayleigh distillation. The authors showed that N loss as N_2 and NH_3 followed Rayleigh distillation would have shifted their $\Delta^{15}N^{alloy-silicate}$ values by ~70 ‰ and ~40 ‰, respectively, which still would not explain their $\Delta^{15}N^{alloy-silicate}$ which were as high as 243 ‰ in magnitude. The percentage of N retained in the experimental products of this study (~38–89 %) was significantly higher

Fig. 8. $\Delta^{15}N^{alloy-silicate}$ as a function of fO_2. **A)** The $\Delta^{15}N^{alloy-silicate}$ values of this study are approximately similar in magnitude to the data of Li et al. (2016) and Shi et al. (2022) but are much smaller than those of Dalou et al. (2019a). Also, $\Delta^{15}N^{alloy-silicate}$ values of this study and Shi et al. (2022) are negatively correlated with $\log fO_2$ whereas those of Dalou et al. (2019a) are positively correlated. **B)** $\Delta^{15}N^{alloy-silicate}$ values of this study, in agreement with the data of Li et al. (2016) and Dalou et al. (2019a), are negative indicating enrichment of alloy melts in lighter isotopes of N during alloy melt-silicate melt equilibration but are in disagreement with those of Shi et al. (2022) where they report increasingly positive $\Delta^{15}N^{alloy-silicate}$ values below ~ IW–1.2. **C)** Solid line represents the best fit of $\Delta^{15}N^{alloy-silicate}$– fO_2 correlation determined by the linear regression of the data of this study and Li et al. (2016). Dashed lines represent the 95 % confidence interval envelope of the regression.

than Dalou et al. (2019a) (~14–42 %). More importantly, unlike in Dalou et al. (2019a), the $\delta^{15}N^{alloy}$ and $\delta^{15}N^{silicate}$ (and consequently, $\Delta^{15}N^{alloy-silicate}$) values reported in this study do not show any correlation with the percentage of N retained despite significant variations in the N deficit. What is the cause behind this disparity? The answer to this question may lie in the details of the experimental setup used for equilibration of N with alloy and silicate melts.

Thermal decomposition of N bearing compounds like iron nitrides, Si_3N_4, etc. is the source of N in experimental studies simulating elemental and isotopic fractionation of N between alloy and silicate melts (Li et al., 2016; Dalou et al., 2017, 2019a; Grewal et al., 2019b, 2019a; Speelmanns et al., 2019; ,2021b; Jackson et al., 2021; Shi et al., 2022). Complete decomposition of the solids results in the formation of a N-bearing vapor phase that equilibrates with alloy and silicate melts (Grewal et al., 2019a; Speelmanns et al., 2019; Jackson et al., 2021). N abundances as well as isotopic compositions of the alloy and silicate melts are therefore set during equilibration with this vapor phase. The vapor, depending upon the porosity of capsule, can potentially diffuse across the capsule walls either prior to or during equilibration with alloy and silicate melts (Grewal et al., 2019a; Speelmanns et al., 2019). All other parameters being similar, N contents in alloy and silicate melts of this study did not vary with experimental duration (Supplementary Fig. 2A, B). A lack of N loss via its diffusion across the capsule walls is also recorded in their N isotopic compositions of alloy and silicate melts: $\delta^{15}N^{alloy}$ and $\delta^{15}N^{silicate}$ values did not show any correlation with experimental duration (Fig. 4). Also, despite their variations, $\delta^{15}N^{alloy}$ and $\delta^{15}N^{silicate}$ values of this study are systematically lower and higher than the N isotopic compositions of the starting materials, respectively (Fig. 9). This observation suggests that diffusion of the vapor phase across the capsule walls was negligible prior to or during its equilibration with alloy and silicate melts.

Storage of N in the capsule pore spaces (which decrease in volume with increasing P) has been postulated as an explanation for the N deficit in the experimental products of alloy and silicate melt equilibration (Speelmanns et al., 2018, 2019; Grewal et al., 2019a). This mechanism could explain the invariance of N contents in alloy and silicate melts as well as $\delta^{15}N^{alloy}$ and $\delta^{15}N^{silicate}$ values in the time series experiments and the experiments with varying amounts of N in the starting mixtures. Consequently, despite variability in N deficit of the experimental products, $\Delta^{15}N^{alloy-silicate}$ values of this study do not show evidence for Rayleigh distillation. Storage of excess N in the capsule walls also attests to the importance of sintering of the capsules at 800–900 °C prior to heating to the target T as it decreases the permeability of the capsules, thereby minimizing the diffusive loss of N vapor across the capsule walls (Grewal et al., 2019a; Jackson et al., 2021). In addition to a lower P range, Dalou et al. (2019a) did not sinter their capsules prior to heating to target T which could have resulted in a higher fraction of N loss (via diffusion of N across the capsule walls during the experimental duration) and the ensuing correlations between $\delta^{15}N^{silicate}$ values and fraction of N retained.

4.4. Effect of fO_2 on $\Delta^{15}N^{alloy-silicate}$

Our data, in agreement with similar experimental data for other moderately volatile and refractory elements like S, Cr, Cu, Si, Mo, and Fe (e.g., Bourdon et al., 2018; Labidi et al., 2016; Shahar et al., 2011), shows that there is limited equilibrium isotopic fractionation between alloy and silicate melts at temperatures applicable for core-mantle differentiation. Due to the lower mass of N and the typically larger fractional mass difference between ^{14}N and ^{15}N relative to the isotopes of heavier elements, the magnitude of N isotope fractionation observed in this study is greater than that observed for heavier elements such as S, Cr, Cu, Si, Mo, and Fe. Although there are no direct estimates on the extent of C isotopic fractionation between alloy and silicate melts, it should be noted that the magnitude of our measured $\Delta^{15}N^{alloy-silicate}$ values is well within the range of the extent of predicted C isotopic fractionation between graphite and alloy melts (2.6 ‰ to 4.5 ‰; Satish-Kumar et al., 2011).

Isotope fractionation is shown to scale with $1/T^2$ at temperatures relevant for core-mantle differentiation in protoplanets and planets provided there are no other changes in the bonding environment of the element of interest in the metallic and silicate phases (Bourdon et al., 2018). However, we did not observe a resolvable correlation between $\Delta^{15}N^{alloy-silicate}$ and T in our temperature series experiments (Fig. 5C). Even though Li et al. (2016) and Shi et al. (2022) did not systematically constrain the effect of T (by holding all other parameters constant) on $\Delta^{15}N^{alloy-silicate}$, they also did not did not observe any correlation between these two parameters. This lack of correlation could either be related to the relatively narrow T range explored in this study, and the studies of Li et al. (2016) and Shi et al. (2022), or masking of the T effect due to small variations in fO_2 and fH_2 in the temperature series experiments, which likely resulted in changes of bonding environment of N in the silicate melts (Armstrong et al., 2015; Mosenfelder et al., 2019; Grewal et al., 2020). Targeted experiments need to be conducted in the future to quantify the effect of T on $\Delta^{15}N^{alloy-silicate}$ values.

$\Delta^{15}N^{alloy-silicate}$ values determined in this study show a clear correlation with $\log fO_2$ – the principle parameter varied (Fig. 8C). Previous studies have shown that partitioning of N between alloy and silicate melts is primarily controlled by the change in the bonding environment of N in the metallic and/or silicate phases as function of fO_2. Is the fO_2 dependent isotopic fractionation of N between alloy and silicate melts also controlled by a similar mechanism? N solubility in alloy melts decreases in the presence of other non-metals – namely S, Si, and C – due to increase in $\gamma_N^{alloy\ melt}$ as a result of non-metal - non-metal non-ideal interactions (Grewal et al., 2019a, 2021b). The starting materials of this study were S-free; therefore, N dissolution in the alloy melts could be affected by the co-presence of Si and C only. Within the fO_2 space explored in this study, there is limited incorporation of Si in the alloy melts (except for one experiment containing 0.44 wt% Si, all experimental alloys contain less than 0.1 wt% Si). The C contents of the graphite-saturated alloys of this study are not correlated with fO_2. The presence of C, therefore, did not result in any inter-experiment variation of N dissolution as a function of fO_2. As a result, a change in the bonding environment of N in the alloy melts is unlikely to cause the variation of $\Delta^{15}N^{alloy-silicate}$ values with fO_2.

N solubility in the silicate melts is known to increase significantly with decreasing fO_2 within the fO_2 space explored in this study (Libourel et al., 2003; Boulliung et al., 2020; Bernadou et al., 2021). A combination of N, C, and H contents along with N—C—O—H speciation (determined using Fourier Transform Infrared (FTIR) and Raman Spectroscopy) has been used previously to constrain the contribution of different N species in silicate glasses as function of fO_2 and fH_2 (Dalou et al., 2019b; Mosenfelder et al., 2019; Grewal et al., 2020). N dissolves as molecular N_2 in oxidized silicate melts whereas at increasingly reduced conditions it starts to chemically combine with the silicate melt structure in the form of reduced species – anhydrous N^{3-} and/or hydrous N—H (Mosenfelder et al., 2019; Grewal et al., 2020). The dissolution of N in the form of these reduced species is the primary cause of the enhanced N solubility in reduced silicate melts. High P-T experiments examining the partitioning of N between alloy and silicate melts have shown that the reduced N species are the dominant form of N dissolution in silicate melts at $\log fO_2$ <~IW–2 to IW–1 (Dalou et al., 2017; Grewal et al., 2019a, 2020). Under those

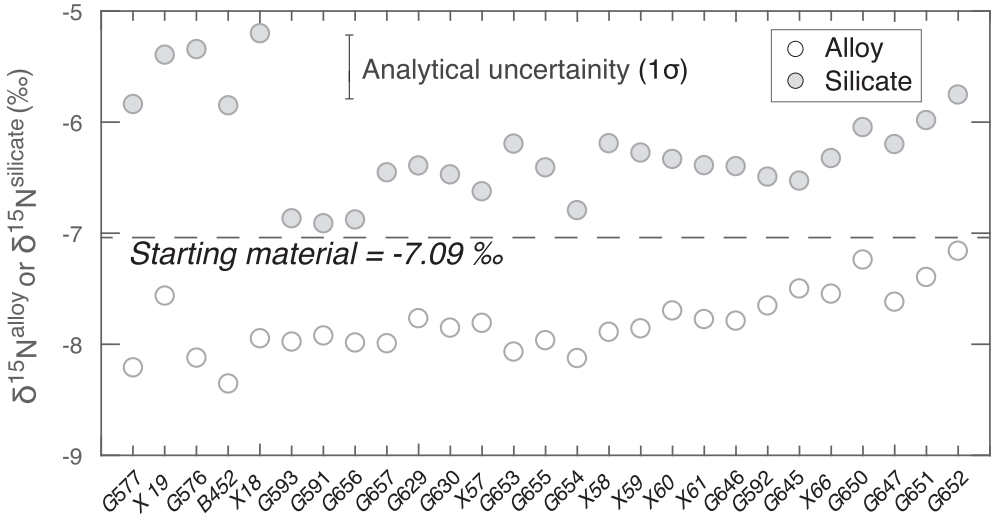

Fig. 9. Nitrogen isotopic composition of alloy and silicate phases relative to the N bearing starting materials. $\delta^{15}N$ values of the starting material is represented by the dashed line. $\delta^{15}N$ values of the alloy and silicate phases are lower and higher relative to the starting materials indicating fractionation of N between the two phases. Analytical uncertainty (1σ) of the $\delta^{15}N$ values is ± 0.3 ‰.

conditions, the relative proportion of different reduced N species depends upon the competition between N content in the silicate melt and the amount of H available to bond with those N atoms (Mosenfelder et al., 2019; Grewal et al., 2020). Bulk H contents in the silicate melts of this study, and other relevant previous studies, are limited due to the nominally water-free character of the starting mixtures. As a result, due to its limited availability, H cannot keep pace to bond with increasing N in the silicate melts as fO_2 decreases (Mosenfelder et al., 2019; Grewal et al., 2020). Therefore, the relative contribution of N species to N dissolution in the silicate melts evolves from molecular NH_3 to Si-bonded NH_2^-, NH^{2-}, and N^{3-} species with decreasing fO_2 (Mosenfelder et al., 2019; Grewal et al., 2020). FTIR analyses – the only method that would yield N speciation data in the fO_2 range of this study – requires polishing of silicate glasses to ~100 μm thickness. This polishing would have resulted in extensive loss of sample volume thereby compromising the N isotopic analyses of the silicate glasses by EA-IRMS. We note that the experimental design, conditions, and materials of this study are almost identical to that of two previous studies from the same lab (Grewal et al., 2019b, 2019a) where the partitioning of N between alloy and silicate melts was constrained with 85 high *P-T* experiments. Grewal et al. (2020) reported FTIR spectroscopic analyses of the silicate glasses of 62 experiments of those two studies and combined FTIR analyses with N and H contents to characterize N species in silicate glasses as a function of fO_2. In this study we indirectly inferred the likely evolution of N speciation in the silicate melts by using the results of Grewal et al. (2020). Also, these results were compared with the spectroscopic analyses of Mosenfelder et al. (2019) – the only other study which systematically determined speciation of N in reduced silicate glasses via FTIR analyses.

Can the change of N speciation in the silicate melts with fO_2 explain the correlation between $\Delta^{15}N^{alloy-silicate}$ and fO_2? To answer this question, we compare the results of our first-principles calculations with those of our experiments. The calculations show that equilibrium N isotopic fractionation of Fe-rich intermetallic crystals relative to N molecules and silicate crystals results in metals containing isotopically lighter N relative to the silicates (Fig. 10A). This prediction is in agreement with the direction of equilibrium N isotopic fractionation between alloy and silicate melts suggested by the present study, Li et al. (2016), and Dalou et al. (2019a). The direction of equilibrium N isotopic fractionation predicted by our first-principles calculations is, however, in complete disagreement with the data of Shi et al. (2022) where positive $\Delta^{15}N^{alloy-silicate}$ values were reported at $\log fO_2$ <-IW–1.2. The magnitude of predicted N isotopic fractionation (1–3.5 ‰) is in quantitative agreement with the range of $\Delta^{15}N^{alloy-silicate}$ values of the present study (1–3.2 ‰) and Li et al. (2016) (1–5.5 ‰), but distinctly smaller than that of Dalou et al. (2019a) (25–243 ‰). In addition to the direction of equilibrium N isotopic fractionation, the magnitude of N isotopic fractionation predicted by our first-principles calculations does not agree with the results of Shi et al. (2022), especially at $\log fO_2$ < IW–1.2, where they reported increasingly larger $\Delta^{15}N^{alloy-silicate}$ values (as high as 10.4 ‰) at more reducing conditions.

We want to point out that even though Fe-rich intermetallic crystals (Fe_3N, Fe_4N, and $Fe_{16}N_2$) crystals are not perfect analogues for the N-bearing alloy melts of this study, there is a consistency in their $1000 \bullet \ln\beta(^{15}N/^{14}N)$ values – all Fe_xN crystals have approximately similar equilibrium N isotopic compositions (Fig. 7). Therefore, it is not unreasonable to assume that alloy melts having similar chemical compositions, i.e., Fe-rich metal with some dissolved N, will have similar isotopic properties. Similar arguments could also be made for the N isotopic properties of the analogues of relevant N species in the silicate melts.

The magnitude of difference in N isotopic fractionation factors is predicted to be highest between Fe-rich intermetallic crystals and N_2 molecules followed by NH_3, $SiO_3H_3NH_2$, $Si_2O_6H_6NH$, and β-Si_3N_4 (Fig. 10A). Even though the effect of fO_2 on $\Delta^{15}N^{alloy-silicate}$ cannot be directly constrained by first principle calculations, $1000 \bullet \ln\beta(^{15}N/^{14}N)$ values of modelled N species can nevertheless be combined with N speciation in experimental silicate melts to predict the magnitude of N isotopic fractionation between alloy and silicate phases as a function of fO_2. As discussed earlier, N speciation in H-poor, magma ocean-like silicate melts evolves from molecular N_2 to NH_3 to Si bonded NH_2^-, NH^{2-}, and N^{3-} species with decreasing fO_2 (Mosenfelder et al., 2019; Grewal et al., 2020). Using this speciation trend as a proxy of changing fO_2, we plotted modelled equilibrium N isotopic fractionation of Fe-rich intermetallic crystals relative to N molecules and silicate crystals between 1600 and 1800 °C (Fig. 10B). The extent of N isotopic fractionation relative to Fe-rich intermetallic crystals decreases uniformly from molecular N_2 (~–3.5 ‰) to β-Si_3N_4 (~–1‰). This trend is in qualitative agreement with the experimental results of this study where $\Delta^{15}N^{alloy-silicate}$ values increase from –3.2 ‰ at $\log fO_2$ ~IW–2 to –1‰ at $\log fO_2$ ~IW–3.2. This trend differs from

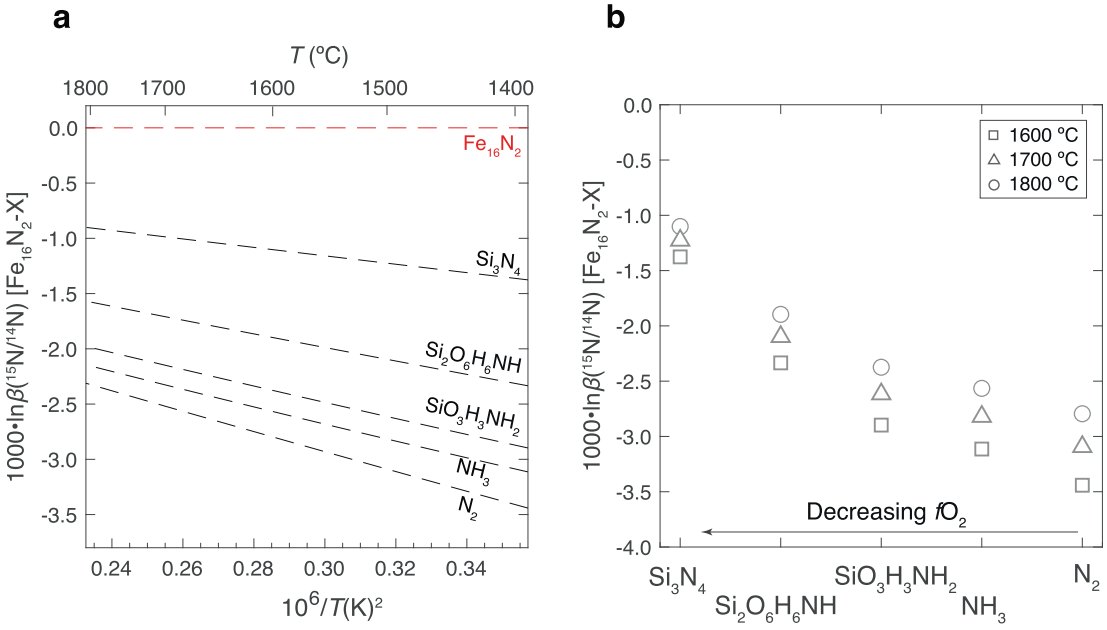

Fig. 10. Calculated equilibrium isotopic fractionation of N between the phases that represent N speciation in the metallic and silicate melts. **A)** Within the *T* range of the experiments of this study, the calculated equilibrium fractionation of N between metals and silicates lies within the range of $\Delta^{15}N^{alloy-silicate}$ values determined in this study. **B)** The calculated fractionation of N between metals and various N species in the silicates qualitatively explains the negative correlation observed between $\Delta^{15}N^{alloy-silicate}$ and fO_2 in Fig. 8C.

that found by Dalou et al. (2019a) in which $\Delta^{15}N^{alloy-silicate}$ values decreased with fO_2. Even though Shi et al. (2022) also report a negative correlation between $\Delta^{15}N^{alloy-silicate}$ and logfO_2, both the direction and magnitude of their N isotopic fractionation is in disagreement with our experimental results and first-principles calculations. Importantly, our first-principles calculations based on the relevant speciation of N in the alloy and silicate melts rule out a change in the direction equilibrium N isotopic fractionation between alloy and silicate melts at more reducing conditions as predicted by Shi et al. (2022). This combined evidence suggests that unlike the experimental data of this study, the $\Delta^{15}N^{alloy-silicate}$ values reported by Shi et al. (2022) do not capture the equilibrium fractionation of N between alloy and silicate melts.

In conclusion, the agreement between experimentally measured and calculated $\Delta^{15}N^{alloy-silicate}$ values of this study suggests that, despite their inherent limitations, the experiments described in the present study did approach equilibrium fractionation of N isotopes between alloy and silicate melts. That is, the equilibration of N vapor phase with alloy and silicate melts most likely occurred in a closed system. More importantly, the magnitude of N isotopic fractionation at high temperatures relevant for core-mantle differentiation, in contrast to Dalou et al. (2019a), is indeed small. It is not possible for us to determine the cause behind the anomalously large magnitude of $\Delta^{15}N^{alloy-silicate}$ values measured by Dalou et al. (2019a), but we hypothesize that it is related to the experimental design and procedure (i.e., lower *P*, lack of sintering, etc.) which could have resulted in continuous loss of N vapor across the capsule walls. The discrepancy between the experimental data of this study backed by first principle calculations and the experimental data of Shi et al. (2022) calls into question the applicability of their $\Delta^{15}N^{alloy-silicate}$ values in capturing equilibrium fractionation of N isotopes during core-mantle differentiation. The cause behind the discrepancy is elusive at this stage and requires future investigation.

4.5. Implications for the origin of nitrogen in protoplanets and planets

Nitrogen isotopic compositions of meteorite and terrestrial samples are an essential tool for tracking the journey of life-essential volatiles from primordial organics to the first-formed protoplanets and eventually to the present-day rocky planets (Füri and Marty, 2015; Grewal, 2022). Due to their undifferentiated character, chondrites are assumed to be the best representatives of primordial materials in the protosolar disk and their N isotopic compositions have been directly used to track the origin of N in rocky planets, including Earth. However, this approach has a couple of crucial limitations. First, the parent bodies of chondrites belonging to the inner (ECs and ordinary chondrites (OCs)) and outer solar system reservoirs (carbonaceous chondrites (CCs)) accreted at timescales greater than ~ 2 Ma after calcium-aluminum-rich inclusions (CAIs) (Sugiura and Fujiya, 2014). Whereas the accretion ages of the parent bodies of iron meteorites in both of these reservoirs suggest that protoplanets began to accrete right at the beginning of the formation of the solar system, i.e., within ~1 Ma after CAIs (Kruijer et al., 2017; Spitzer et al., 2021). Rocky planet formation models predict that the seeds of the present-day rocky planets also began to grow during these timescales (Weidenschilling, 2019; Morbidelli et al., 2022). Therefore, the $^{15}N/^{14}N$ ratios of rather late-accreting chondrite parent bodies may not fully capture the N isotopic compositions of the first-formed protoplanets in the inner and outer regions of the protosolar disk. Second, paleomagnetic data for CV, CM, and Rumuruti chondrites suggest that some, if not all, chondrites sample only the surficial reservoirs of their parent bodies (e.g., Elkins-Tanton et al., 2011; Weiss and Elkins-Tanton, 2013). Also, all chondrites record effects of thermal metamorphism and aqueous alteration (Brearley, 2006; Huss et al., 2006) and their $^{15}N/^{14}N$ ratios are known to be greatly affected by these processes (Sephton et al., 2003; Pearson et al., 2006; Grewal, 2022). For example, unequilibrated OCs and CO and CV chondrites exhibit a decrease in $\delta^{15}N$ values with an increasing degrees of thermal metamorphism (Hashizume and Sugiura, 1995; Pearson et al., 2006). Whereas CI, CM, and CR chondrites exhibit a decrease in $\delta^{15}N$ values with increasing degrees of aqueous alteration (Pearson et al., 2006). Consequently, their $^{15}N/^{14}N$ ratios might not be fully representative of the N isotopic compositions of their bulk bodies (Grewal, 2022).

Iron meteorites provide an alternate pathway to track the N isotopic compositions of the earliest formed rocky bodies in the solar system. Each group of iron meteorite exhibits a distinct average N isotopic composition – with NC irons generally have lower $^{15}N/^{14}N$ ratios relative to CC irons (Grewal et al., 2021c). Evidence till data suggests that the $^{15}N/^{14}N$ ratios within a given group of magmatic iron meteorites were not affected by any secondary processes like volatile degassing and fractional crystallization that resulted in mass dependent fractionation of N isotopes (Franchi et al., 1993; Prombo and Clayton, 1993). As a result, their $^{15}N/^{14}N$ ratios likely capture the mean N isotopic compositions of their parent cores (Grewal et al., 2021c). Nitrogen inventory of the parent cores of magmatic iron meteorites was set during core-mantle differentiation (Grewal et al., 2021c, 2022); therefore their utility in constraining the N isotopic compositions of their bulk bodies is determined by the extent of N isotopic fractionation during alloy melt-silicate melt equilibration. Accounting for the conductive and/or convective thermal evolution of the interiors of the parent bodies of magmatic irons heated by ^{26}Al decay, thermochemical models suggest that these bodies underwent core formation underneath solid, conductive shells (Lichtenberg et al., 2016; Kaminski et al., 2020; Sturtz et al., 2022). Therefore, N fractionation during core formation in the parent bodies of magmatic iron meteorites can be modelled using core-mantle equilibration models without accounting for the atmosphere component (Grewal et al., 2022). Elemental and isotopic fractionation of N between alloy and silicate melts, in combination with the $\delta^{15}N$ values magmatic iron meteorites, can be used to backtrack the N isotopic compositions of their bulk bodies by the following set of equations:

$$\delta^{15}N^{bulk} = \frac{M_{core} \times [N]_{core}}{[M_{core} \times [N]_{core} + M_{mantle} \times [N]_{mantle}]} \times \delta^{15}N^{core} + \frac{M_{mantle} \times [N]_{mantle}}{[M_{core} \times [N]_{core} + M_{mantle} \times [N]_{mantle}]} \times \delta^{15}N^{mantle} \quad (3)$$

$$\Delta^{15}N^{alloy-silicate} = \delta^{15}N^{core} - \delta^{15}N^{mantle} \quad (4)$$

$$D_N^{alloy/silicate} = \frac{[N]_{core}}{[N]_{mantle}} \quad (5)$$

$$r = \frac{M_{core}}{M_{mantle}} \quad (6)$$

Due to the relatively small sizes of the parent bodies of iron meteorites (a few hundreds of kms in diameter; Kaminski et al. (2020)) and low temperatures of core formation (1325-1615 °C; Kruijer et al. (2014)), $\Delta^{15}N^{alloy-silicate}$ values estimated in our study are directly applicable to core-mantle differentiation iron meteorite parent bodies. Limited data for a few iron groups of iron meteorites suggests that core-mantle differentiation in their parent bodies occurred between $\log fO_2$ ~IW–3 and IW–1 (Campbell and Humayun, 2005; Righter et al., 2016). To constrain the variation of $\Delta^{15}N^{alloy-silicate}$ with fO_2, we estimated a simple empirical relationship based on the linear regression of the experimental data of this study and Li et al. (2016) (Fig. 8C):

$$\Delta^{15}N^{alloy-silicate} = -0.96(\pm0.09) \times \log fO_2 - 4.14(\pm0.24) \quad (7)$$

Due to the low C contents of the parent cores of iron meteorites (Hirschmann et al., 2021), we used the parameterized $D_N^{alloy/silicate}$ relationship of Grewal et al. (2021b) to estimate elemental partitioning of N between alloy and silicate melts for C-poor systems. We note, however, that any potential effects of C contents of alloy melts on $\Delta^{15}N^{alloy-silicate}$ is lacking at present and should be investigated in a future study. Core-to-mantle mass ratios (r) of the parent bodies of iron meteorites estimated by Hilton et al. (2022) were used. For other magmatic iron groups for which estimates of core-to-mantle mass ratios are lacking, we used the averaged core-to-mantle mass ratio of the NC and CC reservoirs estimated by Hilton et al. (2022). $\delta^{15}N$ values of different groups of iron meteorites estimated by Grewal et al. (2021c) were used for $\delta^{15}N^{core}$. Due to the uncertainty in the exact fO_2 of their core-mantle differentiation, we estimated the $\delta^{15}N^{bulk}$ for each group of iron meteorites at three discrete $\log fO_2$s (IW–3, IW–2, and IW–1), i.e., based on the primary control of fO_2 on elemental and isotopic fractionation of N between alloy and silicate melts. We note that even though our model calculations are directly applicable for the parent bodies of magmatic iron meteorites, we have also calculated the $\delta^{15}N^{bulk}$ of the two non-magmatic iron groups (IAB-MG,sL and IIE) for comparison.

Our model calculations show that $\delta^{15}N^{bulk}$ for each group of iron meteorites increases slightly with decreasing fO_2 (Fig. 11). This decrease is a result of a decrease in $D_N^{alloy/silicate}$ by an order of magnitude with decreasing $\log fO_2$ from IW to 1 to IW–3. Therefore, the fraction of the bulk N inventory that is present in the core decreases with decreasing $\log fO_2$ manifesting in a larger difference in the N isotopic compositions of the bulk and core. However, even at IW–3, $\delta^{15}N^{bulk}$ is not >0.5 ‰ higher than the $\delta^{15}N^{core}$ for any given group of iron meteorites. Therefore, a combination of high $D_N^{alloy/silicate}$ within the fO_2 of the core-mantle differentiation of iron meteorite parent bodies along with low $\Delta^{15}N^{alloy-silicate}$ values confirms that the $\delta^{15}N$ values of iron meteorites are broadly representative of the N isotopic compositions of their bulk bodies. More importantly, these calculations suggest that variation in the N isotopic compositions of planetesimals in the protosolar disk could be larger than that predicted by chondrites (Fig. 1). Even though the $\delta^{15}N$ values ratios of CC chondrites and iron meteorites cover the same range (up to 200 ‰), NC iron meteorites have much lower $\delta^{15}N$ values (lower limit of –95 ‰) relative to ECs (lower limit of –27 ‰). Therefore, NC iron meteorites capture a larger variation in the N isotopic compositions of inner solar system planetesimals relative to ECs. As Earth and other rocky planets in the

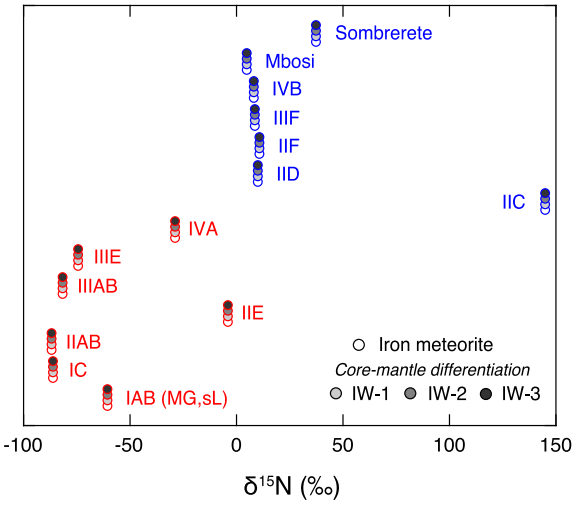

Fig. 11. Comparison of the mean $\delta^{15}N$ of different groups of iron meteorites (white circles) with the predicted $\delta^{15}N$ values of their parent bodies as a result of core-mantle differentiation at $\log fO_2$ = IW–3 (black), IW–2 (dark grey), and IW–1 (light grey). The predicted bulk $\delta^{15}N$ values are almost identical to the $\delta^{15}N$ of iron meteorites irrespective of the fO_2 of core-mantle differentiation. Note that this plot does not have any parameter on the Y-axis. For each group of iron meteorites, the circles are offset from each other to reflect the relatively small differences in the mean $\delta^{15}N$ of iron meteorites and the calculated $\delta^{15}N$ values of their parent bodies at three different fO_2s (IW–3, IW–2, and IW–1). Blue and red symbols depict the origins of iron meteorite groups from CC and NC reservoirs, respectively. (For interpretation of the references to colour in this figure legend, the reader is referred to the web version of this article.)

inner solar system largely grew via the accretion of NC planetesimals, using the $\delta^{15}N$ values of ECs as representative of NC reservoir-derived planetesimals substantially underestimates the contribution of ^{15}N-rich materials to the present-day N budget of rocky planets.

The results of this study have fundamental implications for the origin of N in the Earth. Earth's growth was likely fed by accretion of differentiated protoplanets of variable oxidation state whose cores could have undergone variable degrees of equilibration with proto-Earth's mantle (Rubie et al., 2011). Also, the collisional accretion of these impactors would have led to the formation of surficial MOs, leading to the degassing of N into the atmosphere, which would result in the fractionation of N isotopes between vapor and silicate melts (Dalou et al., 2022). However, the fate of these MO degassed atmospheres during the collisional growth of Earth is poorly constrained (Schlichting et al., 2015). Additionally, the contribution of late accretion to the N budget of the Earth (i.e., fraction of N in the BSE that did not participate in a core-mantle differentiation event in Earth) is also uncertain (Hirschmann, 2016). These factors make it rather difficult to quantitatively track the N isotopic composition of the BSE during its entire growth history. Despite these uncertainties, it has been shown that the N isotopic composition of the BSE shows a dichotomy with the primitive mantle being distinctly ^{15}N-poor (average $\delta^{15}N = \sim -5‰$; Cartigny and Marty (2013)) relative to the atmosphere ($\delta^{15}N = 0$ ‰). This difference in reservoir signatures has been used as an evidence for a dual source of Earth's N, with the interior and atmosphere inheriting a majority of their N inventory from EC-like and CC-like materials, respectively (Javoy, 1997; Marty, 2012; Piani et al., 2020; Grewal et al., 2021c). Based on their large measured fractionation of N isotopes between alloy and silicate melts, Dalou et al. (2019a) suggested that core-mantle differentiation alone during Earth's growth could increase the $\delta^{15}N$ values of its mantle to its present-day value even if EC-like materials alone supplied the entire N inventory of Earth's interior. However, the findings of this study suggest otherwise: fractionation of N isotopes between alloy and silicate melts during any given accretion event must be limited. As a result, core-mantle differentiation should not have left large imprints on the N isotopic composition of the BSE. Therefore, $\delta^{15}N$ of the Earth's primitive mantle primarily reflects the N isotopic composition of the Earth's accreting materials rather than that of core-mantle differentiation as suggested by Dalou et al. (2019a).

A limited fractionation of N isotopes during core-mantle differentiation suggests that $\delta^{15}N$ values of Earth's primitive mantle cannot be solely explained by the accretion of EC-like materials. This issue becomes even more compounded as $\delta^{15}N$ values of ^{15}N-poor NC iron meteorite groups like IAB-MG, IC, IIAB, IIIAB, and IIIE, rather than ECs, capture the variation of N isotopes in the inner solar system planetesimals. An accretion of relatively ^{15}N-rich materials is therefore necessary to explain the N isotopic composition of Earth's primitive mantle. It is difficult to constrain the timing of accretion of the ^{15}N-rich materials due to uncertainties involved in constraining the volatile loss during Earth's growth. However, the presence of nitrogen during the entire accretion history of Earth, suggests that life-essential volatiles were widely available during the growth of rocky planets. Therefore, the volatile-poor nature of Earth and other rocky planets is not determined by the lack of their availability but instead by volatile loss, either during protoplanetary differentiation or during planetary growth (Grewal et al., 2021b, 2022; Hirschmann et al., 2021; Grewal, 2022).

5. Concluding remarks

We used multiple sets of high *P-T* experiments to constrain equilibrium N isotopic fractionation at oxygen fugacities relevant to core-mantle differentiation in rocky protoplanets and planets. We show that the fractionation of N isotopes between alloy and silicate melts is indeed small ($\Delta^{15}N^{alloy-silicate} = -3.3$ ‰ to -1.0 ‰ at $\log fO_2$ = IW–3.77 to IW–1.70, respectively) rather than large. *Ab initio* calculations accounting for the variation in the speciation of N in silicate melts as a function of fO_2 confirm both the magnitude and direction of N isotopic fractionation as predicted by our high *P-T* experiments. The discrepancy between the experimental data of this study backed by first principle calculations and the experimental data of Dalou et al. (2019a) and Shi et al. (2022) suggests that the $\Delta^{15}N^{alloy-silicate}$ values of these two studies do not capture equilibrium fractionation of N isotopes during core-mantle differentiation.

Our data suggests that at the high temperatures relevant for core-mantle differentiation in rocky protoplanets and planets, fractionation of N between alloy and silicate melts should not leave any significant imprints on the N isotopic compositions of their resulting cores and mantles. As a result, $\delta^{15}N$ values of either cores or bulk silicate reservoirs of differentiated rocky bodies are representative of their bulk N isotopic compositions. For instance, $\delta^{15}N$ values of iron meteorites and the BSE are representative of their bulk bodies (provided no other processes substantially affected the N isotopic signatures post core-mantle differentiation). We predict that iron meteorites, in addition to chondrites, can be used to track the variation in the N isotopic compositions of the first formed rocky bodies of the solar system. Because $\delta^{15}N$ values of some NC iron meteorites are much lower than that of ECs, we suggest that the variation in the N isotopic compositions of inner solar-system planetesimals was larger than what is inferred from ECs alone. Earth's growth primarily via the accretion of similar planetesimals and a relatively high $\delta^{15}N$ of present-day Earth's primitive mantle (–5‰) compared to NC iron meteorites necessitates a significant contribution of ^{15}N-rich materials to the Earth's interior.

Data availability

All data is shared in the supplementary files

Declaration of Competing Interest

The authors declare that they have no known competing financial interests or personal relationships that could have appeared to influence the work reported in this paper.

Acknowledgements

Amrita P. Vyas is thanked for helping improve the clarity of our communication. Gelu Costin is thanked for his assistance during the microprobe analysis. We are grateful to have received thorough and constructive reviews by Mathieu Roskosz and two anonymous reviewers which significantly helped us improved the manuscript. We also thank Mathieu Roskosz for his efficient handling of the manuscript as an Associate Editor. D.S.G. received support from a Barr Foundation Postdoctoral Fellowship by California Institute of Technology, a NASA FINESST grant 80NSSC19K1538, and a Lodieska Stockbridge Vaughn Fellowship by Rice University. T.S. received support from NASA grant 80NSSC19K0784. R.D. received support from NASA grants 80NSSC18K0828 and 80NSSC18K1314. E.S. received support from NSF grants EAR1524811 and EAR1530306.

Appendix A. Supplementary material

Supplementary material to this article can be found online at https://doi.org/10.1016/j.gca.2022.10.025.

References

Alexander, C.M.O., Cody, G.D., de Gregorio, B.T., Nittler, L.R., Stroud, R.M., 2017. The nature, origin and modification of insoluble organic matter in chondrites, the major source of Earth's C and N. Geochemistry 77, 227–256.

Armstrong, L.S., Hirschmann, M.M., Stanley, B.D., Falksen, E.G., Jacobsen, S.D., 2015. Speciation and solubility of reduced C-O-H-N volatiles in mafic melt: Implications for volcanism, atmospheric evolution, and deep volatile cycles in the terrestrial planets. Geochim. Cosmochim. Acta 171, 283–302.

Bernadou, F., Gaillard, F., Füri, E., Marrocchi, Y., Slodczyk, A., 2021. Nitrogen solubility in basaltic silicate melt - Implications for degassing processes. Chem. Geol. 573, 120192.

Bigeleisen, J., Mayer, M.G., 1947. Calculation of Equilibrium Constants for Isotopic Exchange Reactions. J. Chem. Phys. 15, 261–267.

Boulliung, J., Füri, E., Dalou, C., Tissandier, L., Zimmermann, L., Marrocchi, Y., 2020. Oxygen fugacity and melt composition controls on nitrogen solubility in silicate melts. Geochim. Cosmochim. Acta 284, 120–133.

Bourdon, B., Roskosz, M., Hin, R.C., 2018. Isotope tracers of core formation. Earth Sci. Rev. 181, 61–81.

Brearley, A.J., 2006. The action of water. In: Lauretta, D.S., McSween, H.Y. (Eds.), Meteorites and the Early Solar System II. The University of Arizona Press, Tucson, pp. 587–624.

Brockhouse, B.N., Abou-Helal, H.E., Hallman, E.D., 1967. Lattice vibrations in iron at 296°K. Solid State Commun. 5, 211–216.

Budde, G., Burkhardt, C., Kleine, T., 2019. Molybdenum isotopic evidence for the late accretion of outer Solar System material to Earth. Nat. Astron 3, 736–741.

Campbell, A.J., Humayun, M., 2005. Compositions of group IVB iron meteorites and their parent melt. Geochim. Cosmochim. Acta 69, 4733–4744.

Cartigny, P., Marty, B., 2013. Nitrogen Isotopes and Mantle Geodynamics: The Emergence of Life and the Atmosphere-Crust-Mantle Connection. Elements 9, 359–366.

Dalou, C., Deligny, C., Füri, E., 2022. Nitrogen isotope fractionation during magma ocean degassing: tracing the composition of early Earth's atmosphere. Geochem Perspect Lett, 27–31.

Dalou, C., Füri, E., Deligny, C., Piani, L., Caumon, M.-C., Laumonier, M., Boulliung, J., Edén, M., 2019a. Redox control on nitrogen isotope fractionation during planetary core formation. PNAS 116, 14485–14494.

Dalou, C., Hirschmann, M.M., von der Handt, A., Mosenfelder, J., Armstrong, L.S., 2017. Nitrogen and carbon fractionation during core–mantle differentiation at shallow depth. Earth Planet. Sci. Lett. 458, 141–151.

Dalou, C., Hirschmann, M.M., Jacobsen, S.D., le Losq, C., 2019b. Raman spectroscopy study of C-O-H-N speciation in reduced basaltic glasses: Implications for reduced planetary mantles. Geochim. Cosmochim. Acta 265, 32–47.

Dasgupta, R., Grewal, D.S., 2019. Origin and Early Differentiation of Carbon and Associated Life-Essential Volatile Elements on Earth. In: Orcutt, B., Daniel, I., Dasgupta, R. (Eds.), Deep Carbon: Past to Present. Cambridge University Press, pp. 4–39.

Dasgupta, R., Falksen, E., Pal, A., Sun, C., 2022. The fate of nitrogen during parent body partial melting and accretion of the inner solar system bodies at reducing conditions. Geochim. Cosmochim. Acta 336, 291–307.

Elcombe, M.M., Hulston, J.R., 1975. Calculation on sulphur isotope fractionation between sphalerite and galena using lattice dynamics. Earth Planet. Sci. Lett. 28, 172–180.

Elkins-Tanton, L.T., Weiss, B.P., Zuber, M.T., 2011. Chondrites as samples of differentiated planetesimals. Earth Planet. Sci. Lett. 305, 1–10.

Franchi, I.A., Wright, I.P., Pillinger, C.T., 1993. Constraints on the formation conditions of iron meteorites based on concentrations and isotopic compositions of nitrogen. Geochim. Cosmochim. Acta 57, 3105–3121.

Füri, E., Marty, B., 2015. Nitrogen isotope variations in the Solar System. Nat. Geosci. 8, 515–522.

Giannozzi, P., Baroni, S., Bonini, N., Calandra, M., Car, R., Cavazzoni, C., Ceresoli, D., Chiarotti, G.L., Cococcioni, M., Dabo, I., Dal Corso, A., de Gironcoli, S., Fabris, S., Fratesi, G., Gebauer, R., Gerstmann, U., Gougoussis, C., Kokalj, A., Lazzeri, M., Martin-Samos, L., Marzari, N., Mauri, F., Mazzarello, R., Paolini, S., Pasquarello, A., Paulatto, L., Sbraccia, C., Scandolo, S., Sclauzero, G., Seitsonen, A.P., Smogunov, A., Umari, P., Wentzcovitch, R.M., 2009. QUANTUM ESPRESSO: a modular and open-source software project for quantum simulations of materials. J. Phys.: Condens. Matter 21, 395502.

Goodeve, C., Jack, K.H., 1948. Kinetics of nitrogen evolution from an iron-nitrogen interstitial alloy. Discuss. Faraday Soc. 4, 82.

Grady, M.M., Wright, I.P., Carr, L.P., Pillinger, C.T., 1986. Compositional differences in enstatite chondrites based on carbon and nitrogen stable isotope measurements. Geochim. Cosmochim. Acta 50, 2799–2813.

Grewal, D.S., 2022. Origin of Nitrogen Isotopic Variations in the Rocky Bodies of the Solar System. Astrophys J. 937, 123.

Grewal, D.S., Dasgupta, R., Holmes, A.K., Costin, G., Li, Y., Tsuno, K., 2019a. The fate of nitrogen during core-mantle separation on Earth. Geochim. Cosmochim. Acta 251, 87–115.

Grewal, D.S., Dasgupta, R., Sun, C., Tsuno, K., Costin, G., 2019b. Delivery of carbon, nitrogen, and sulfur to the silicate Earth by a giant impact. Sci. Adv. 5, eaau3669.

Grewal, D.S., Dasgupta, R., Farnell, A., 2020. The speciation of carbon, nitrogen, and water in magma oceans and its effect on volatile partitioning between major reservoirs of the Solar System rocky bodies. Geochim. Cosmochim. Acta 280, 281–301.

Grewal, D.S., Dasgupta, R., Aithala, S., 2021a. The effect of carbon concentration on its core-mantle partitioning behavior in inner Solar System rocky bodies. Earth Planet. Sci. Lett. 571, 117090.

Grewal, D.S., Dasgupta, R., Hough, T., Farnell, A., 2021b. Rates of protoplanetary accretion and differentiation set nitrogen budget of rocky planets. Nat. Geosci. 14, 369–376.

Grewal, D.S., Dasgupta, R., Marty, B., 2021c. A very early origin of isotopically distinct nitrogen in inner Solar System protoplanets. Nat. Astron 5, 356–364.

Grewal, D.S., Seales, J.D., Dasgupta, R., 2022. Internal or external magma oceans in the earliest protoplanets – Perspectives from nitrogen and carbon fractionation. Earth Planet. Sci. Lett. 598, 117847.

Hashizume, K., Sugiura, N., 1995. Nitrogen isotopes in bulk ordinary chondrites. Geochim. Cosmochim. Acta 59, 4057–4069.

Hevey, P.J., Sanders, I.S., 2006. A model for planetesimal meltdown by 26 Al and its implications for meteorite parent bodies. Meteorit. Planet. Sci. 41, 95–106.

Hilton, C.D., Ash, R.D., Walker, R.J., 2022. Chemical characteristics of iron meteorite parent bodies. Geochim. Cosmochim. Acta 318, 112–125.

Hirschmann, M.M., 2016. Constraints on the early delivery and fractionation of Earth's major volatiles from C/H, C/N, and C/S ratios. Am. Mineral. 101, 540–553.

Hirschmann, M.M., Bergin, E.A., Blake, G.A., Ciesla, F.J., Li, J., 2021. Early volatile depletion on planetesimals inferred from C–S systematics of iron meteorite parent bodies. PNAS 118. e2026779118.

Holzheid, A., Palme, H., Chakraborty, S., 1997. The activities of NiO, CoO and FeO in silicate melts. Chem. Geol. 139, 21–38.

Huss, G.R., Rubin, A.E., Grossman, J.N., 2006. Thermal Metamorphism in Chondrites. In: Lauretta, D.S., McSween Jr., H.Y. (Eds.), Meteorites and the early solar system II. University of Arizona Press, pp. 567–586.

Jackson, C.R.M., Cottrell, E., Du, Z., Bennett, N.R., Fei, Y., 2021. High pressure redistribution of nitrogen and sulfur during planetary stratification. Geochem. Perspect. Lett., 37–42.

Javoy, M., 1997. The major volatile elements of the Earth: Their origin, behavior, fate. Geophys. Res. Lett. 24, 177–180.

Kaminski, E., Limare, A., Kenda, B., Chaussidon, M., 2020. Early accretion of planetesimals unraveled by the thermal evolution of the parent bodies of magmatic iron meteorites. Earth Planet. Sci. Lett. 548, 116469.

Kruijer, T.S., Burkhardt, C., Budde, G., Kleine, T., 2017. Age of Jupiter inferred from the distinct genetics and formation times of meteorites. PNAS 201704461.

Kruijer, T.S., Touboul, M., Fischer-Godde, M., Bermingham, K.R., Walker, R.J., Kleine, T., 2014. Protracted core formation and rapid accretion of protoplanets. Science (1979) 344, 1150–1154.

Kubik, E., Sossi, P.A., Siebert, J., Inglis, E., Roskosz, M., Siciliano, R.E., Wehr, N., Moynier, F., 2022. The absence of an effect of nickel on iron isotope fractionation during core formation. Geochim. Cosmochim. Acta 327, 186–199.

Labidi, J., Cartigny, P., Moreira, M., 2013. Non-chondritic sulphur isotope composition of the terrestrial mantle. Nature 501.

Labidi, J., Shahar, A., le Losq, C., Hillgren, V.J., Mysen, B.O., Farquhar, J., 2016. Experimentally determined sulfur isotope fractionation between metal and silicate and implications for planetary differentiation. Geochim. Cosmochim. Acta.

Lengauer, W., Bauer, J., Guillou, A., Ansel, D., Bars, J.P., Bohn, M., Etchessahar, E., Debuigne, J., Ettmayer, P., 1992. WDS-EPMA nitrogen profile determination in TiN/Ti diffusion couples using homotypic standard materials. Mikrochim. Acta 107, 303–310.

Li, L., He, Y., Zhang, Z., Liu, Y., 2021a. Nitrogen isotope fractionations among gaseous and aqueous NH4+, NH3, N2, and metal-ammine complexes: Theoretical calculations and applications. Geochim. Cosmochim. Acta 295, 80–97.

Li, Y., Marty, B., Shcheka, S., Zimmermann, L., Keppler, H., 2016. Nitrogen isotope fractionation during terrestrial core-mantle separation. Geochem Perspect Lett, 138–147.

Li, Y., Li, L., Wu, Z., 2021b. First-principles calculations of equilibrium nitrogen isotope fractionations among aqueous ammonium, silicate minerals and salts. Geochim. Cosmochim. Acta 297, 220–232.

Libourel, G., Marty, B., Humbert, F., 2003. Nitrogen solubility in basaltic melt. Part I. Effect of oxygen fugacity. Geochim. Cosmochim. Acta 67, 4123–4135.

Lichtenberg, T., Golabek, G.J., Gerya, T.v., Meyer, M.R., 2016. The effects of short-lived radionuclides and porosity on the early thermo-mechanical evolution of planetesimals. Icarus 274, 350–365.

Liu, Q., Liu, Y., 2016. Clumped-isotope signatures at equilibrium of CH4, NH3, H2O, H2S and SO2. Geochim. Cosmochim. Acta 175, 252–270.

Marty, B., 2012. The origins and concentrations of water, carbon, nitrogen and noble gases on Earth. Earth Planet. Sci. Lett. 313–314, 56–66.

Méheut, M., Lazzeri, M., Balan, E., Mauri, F., 2007. Equilibrium isotopic fractionation in the kaolinite, quartz, water system: Prediction from first-principles density-functional theory. Geochim. Cosmochim. Acta 71, 3170–3181.

Morbidelli, A., Baillié, K., Batygin, K., Charnoz, S., Guillot, T., Rubie, D.C., Kleine, T., 2022. Contemporary formation of early Solar System planetesimals at two distinct radial locations. Nat. Astron 6, 72–79.

Mosenfelder, J.L., von der Handt, A., Füri, E., Dalou, C., Hervig, R.L., Rossman, G.R., Hirschmann, M.M., 2019. Nitrogen incorporation in silicates and metals: Results from SIMS, EPMA, FTIR, and laser-extraction mass spectrometry. Am. Mineral. 104, 31–46.

Neumann, W., Breuer, D., Spohn, T., 2012. Differentiation and core formation in accreting planetesimals. A & A 543, A141.

Pearson, V.K., Sephton, M.A., Franchi, I.A., Gibson, J.M., Gilmour, I., 2006. Carbon and nitrogen in carbonaceous chondrites: Elemental abundances and stable isotopic compisitions. Meteorit. Planet. Sci. 41, 1899–1918.
Perdew, J.P., Burke, K., Ernzerhof, M., 1996. Generalized Gradient Approximation Made Simple. Phys. Rev. Lett. 77, 3865–3868.
Piani, L., Marrocchi, Y., Rigaudier, T., Vacher, L.G., Thomassin, D., Marty, B., 2020. Earth's water may have been inherited from material similar to enstatite chondrite meteorites. Science (1979) 369, 1110–1113.
Poitrasson, F., Roskosz, M., Corgne, A., 2009. No iron isotope fractionation between molten alloys and silicate melt to 2000 °C and 7.7 GPa: Experimental evidence and implications for planetary differentiation and accretion. Earth Planet. Sci. Lett. 278, 376–385.
Prandini, G., Marrazzo, A., Castelli, I.E., Mounet, N., Passaro, E., Marzari, N., 2021. A Standard Solid State Pseudopotentials (SSSP) library optimized for precision and efficiency. Materials Cloud Archive 2021, 76.
Prombo, C.A., Clayton, R.N., 1993. Nitrogen isotopic compositions of iron meteorites. Geochim. Cosmochim. Acta 57, 3749–3761.
Richet, P., Bottinga, Y., Javoy, M., 1977. A Review of Hydrogen, Carbon, Nitrogen, Oxygen, Sulphur, and Chlorine Stable Isotope Fractionation Among Gaseous Molecules. Annu. Rev. Earth Planet. Sci. 5, 65–110.
Righter, K., Sutton, S.R., Danielson, L., Pando, K., Newville, M., 2016. Redox variations in the inner solar system with new constraints from vanadium XANES in spinels. Am. Mineral. 101, 1928–1942.
Roskosz, M., Bouhifd, M.A., Jephcoat, A.P., Marty, B., Mysen, B.O., 2013. Nitrogen solubility in molten metal and silicate at high pressure and temperature. Geochim. Cosmochim. Acta 121, 15–28.
Rubie, D.C., Frost, D.J., Mann, U., Asahara, Y., Nimmo, F., Tsuno, K., Kegler, P., Holzheid, A., Palme, H., 2011. Heterogeneous accretion, composition and core-mantle differentiation of the Earth. Earth Planet. Sci. Lett. 301, 31–42.
Satish-Kumar, M., So, H., Yoshino, T., Kato, M., Hiroi, Y., 2011. Experimental determination of carbon isotope fractionation between iron carbide melt and carbon: 12C-enriched carbon in the Earth's core?. Earth Planet. Sci. Lett. 310, 340–348.
Schauble, E.A., Ghosh, P., Eiler, J.M., 2006. Preferential formation of 13C–18O bonds in carbonate minerals, estimated using first-principles lattice dynamics. Geochim. Cosmochim. Acta 70, 2510–2529.
Schlichting, H.E., Sari, R., Yalinewich, A., 2015. Atmospheric mass loss during planet formation: The importance of planetesimal impacts. Icarus 247, 81–94.
Sephton, M.A., Verchovsky, A.B., Bland, P.A., Gilmour, I., Grady, M.M., Wright, I.P., 2003. Investigating the variations in carbon and nitrogen isotopes in carbonaceous chondrites. Geochim. Cosmochim. Acta 67, 2093–2108.
Shahar, A., Hillgren, V.J., Young, E.D., Fei, Y., Macris, C.A., Deng, L., 2011. High-temperature Si isotope fractionation between iron metal and silicate. Geochim. Cosmochim. Acta 75, 7688–7697.
Shahar, A., Elardo, S.M., Macris, C.A., 2017. Equilibrium Fractionation of Non-traditional Stable Isotopes: an Experimental Perspective. Rev. Mineral. Geochem. 82, 65–83.
Shi, L., Lu, W., Kagoshima, T., Sano, Y., Gao, Z., Du, Z., Liu, Y., Fei, Y., Li, Y., 2022. Nitrogen isotope evidence for Earth's heterogeneous accretion of volatiles. Nat. Commun. 13, 4769.
Speelmanns, I.M., Schmidt, M.W., Liebske, C., 2018. Nitrogen Solubility in Core Materials. Geophys. Res. Lett. 45, 7434–7443.
Speelmanns, I.M., Schmidt, M.W., Liebske, C., 2019. The almost lithophile character of nitrogen during core formation. Earth Planet. Sci. Lett. 510, 186–197.
Spitzer, F., Burkhardt, C., Nimmo, F., Kleine, T., 2021. Nucleosynthetic Pt isotope anomalies and the Hf-W chronology of core formation in inner and outer solar system planetesimals. Earth Planet. Sci. Lett. 576, 117211.
Sturtz, C., Limare, A., Chaussidon, M., Kaminski, É., 2022. Structure of differentiated planetesimals: A chondritic fridge on top of a magma ocean.
Sugiura, N., Fujiya, W., 2014. Correlated accretion ages and ε 54 Cr of meteorite parent bodies and the evolution of the solar nebula. Meteorit. Planet. Sci. 49, 772–787.
Tsuno, K., Dasgupta, R., 2011. Melting phase relation of nominally anhydrous, carbonated pelitic-eclogite at 2.5-3.0 GPa and deep cycling of sedimentary carbon. Contrib. Miner. Petrol. 161, 743–763.
Walker, D., Dasgupta, R., Li, J., Buono, A., 2013. Nonstoichiometry and growth of some Fe carbides. Contrib. Miner. Petrol. 166, 935–957.
Warren, P.H., 2011. Stable-isotopic anomalies and the accretionary assemblage of the Earth and Mars: A subordinate role for carbonaceous chondrites. Earth Planet. Sci. Lett. 311, 93–100.
Weidenschilling, S.J., 2019. Accretion of the asteroids: Implications for their thermal evolution. Meteorit. Planet. Sci. 54, 1115–1132.
Weiss, B.P., Elkins-Tanton, L.T., 2013. Differentiated Planetesimals and the Parent Bodies of Chondrites. Annu. Rev. Earth Planet. Sci. 41, 529–560.